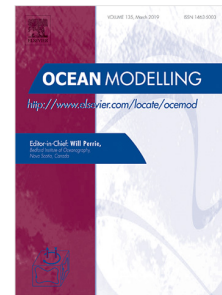


Journal Pre-proof

Performance evaluation of a global CMIP6 single forcing, multi wave model ensemble of wave climate simulations

Gil Lemos, Alvaro Semedo, Rajesh Kumar, Mikhail Dobrynin, Adem Akpınar, Bahareh Kamranzad, Jean Bidlot, Hector Lobeto



PII: S1463-5003(23)00078-1

DOI: <https://doi.org/10.1016/j.ocemod.2023.102237>

Reference: OCEMOD 102237

To appear in: *Ocean Modelling*

Received date: 15 January 2023

Revised date: 26 June 2023

Accepted date: 27 June 2023

Please cite this article as: G. Lemos, A. Semedo, R. Kumar et al., Performance evaluation of a global CMIP6 single forcing, multi wave model ensemble of wave climate simulations. *Ocean Modelling* (2023), doi: <https://doi.org/10.1016/j.ocemod.2023.102237>.

This is a PDF file of an article that has undergone enhancements after acceptance, such as the addition of a cover page and metadata, and formatting for readability, but it is not yet the definitive version of record. This version will undergo additional copyediting, typesetting and review before it is published in its final form, but we are providing this version to give early visibility of the article. Please note that, during the production process, errors may be discovered which could affect the content, and all legal disclaimers that apply to the journal pertain.

© 2023 The Author(s). Published by Elsevier Ltd. This is an open access article under the CC BY license (<http://creativecommons.org/licenses/by/4.0/>).

1 **Performance Evaluation of a Global CMIP6 Single Forcing,**
2 **Multi Wave Model Ensemble of Wave Climate Simulations**

3
4
5 Gil Lemos^{1*}

6 Alvaro Semedo²

7 Rajesh Kumar³

8 Mikhail Dobrynin⁴

9 Adem Akpınar⁵

10 Bahareh Kamranzad⁶

11 Jean Bidlot⁷

12 Hector Lobeto⁸

13
14
15 ¹ Universidade de Lisboa, Faculdade de Ciências, Instituto Dom Luiz, Lisboa, Portugal

16 ² IHE Delft, Department of Coastal, Urban Risk and Resilience, Westvest 7, 2611 AX Delft, The
17 Netherlands

18 ³ Centre for Climate Research Singapore, 36 Kim Chuan Rd, Singapore 537054, Singapore

19 ⁴ Helmholtz-Zentrum Geesthacht Centre for Materials and Coastal Research, Geesthacht, Germany

20 ⁵ Department of Civil Engineering, Bursa Uludag University, Bursa, Turkey

21 ⁶ Department of Civil and Environmental Engineering, University of Strathclyde, Glasgow, G11XJ, United
22 Kingdom

23 ⁷ European Centre for Medium-range Weather Forecasts (ECMWF), Reading RG2 9AX, UK

24 ⁸ IHCantabria - Instituto de Hidráulica Ambiental de la Universidad de Cantabria, Santander, Spain

25
26 * Corresponding author: grlemos@fc.ul.pt
27
28

29 **Keywords:** CMIP6, ensemble, wave climate, simulations, evaluation, uncertainty

30 **Abstract**

31 A performance evaluation is conducted for a state-of-the-art Coupled Model
32 Intercomparison Project Phase 6 (CMIP6)-derived ensemble of global wave climate
33 simulations. A single-model (forcing), single-scenario approach is considered to build the
34 ensemble, where the differentiating factor between each member is the wave model or
35 physics parameterization used to simulate waves. The 7-member ensemble is evaluated
36 for the 1995-2014 historical period, highlighting the impact of the multiple source terms
37 on its robustness. The ensemble's ability to accurately represent the present wave climate
38 is assessed through an extensive comparison with long-term ERA5 reanalysis and *in-situ*
39 observational data. Relevant aspects such as the depiction of extremes and natural wave
40 climate variability are analyzed, and inter-member uncertainties are quantified. Overall,
41 the results indicate that the ensemble is able to accurately simulate the global wave
42 climate, regarding the significant wave height (H_S), mean and peak wave periods (T_m and
43 T_p , respectively) and mean wave direction (MWD). However, we show that using
44 multiple wave models and parameterizations should be cautiously considered when
45 building ensembles, even under the same forcing conditions. Model-parameterization-
46 induced ensemble spreads during the historical period are found to be high, compromising
47 the robustness of projected changes in wave parameters towards the end of the 21st
48 century across several areas of the global ocean.

49

1. Introduction

50 Ocean surface gravity waves (also commonly named “wind waves”) are generated
51 by the action of the wind over the water (Jeffreys, 1924; 1925). These (henceforth just
52 “waves”) are almost always present at the sea surface, in the form of seas, swells, or a
53 combination of them, being a clear part of the climate system (Cavaleri *et al.*, 2012;
54 Babanin *et al.*, 2012) and responsible for modulating the exchange of radiation, heat, mass
55 and momentum between the atmosphere and the ocean (Sullivan *et al.*, 2008; Hogstrom
56 *et al.*, 2009, 2011; Semedo *et al.*, 2009; Rutgersson *et al.*, 2010).

57 Waves play an important role in engineering and environmental issues, as well as in
58 human activities, with direct impacts on coastal dynamics (*e.g.*, Cazenave and Cozannet,
59 2014; Melet *et al.*, 2018; Shih *et al.*, 1995; Ruggiero *et al.*, 2001), shoreline stability
60 (Harley *et al.*, 2017; Barnard *et al.*, 2015; 2017), coastal flooding and sea level extremes
61 (De Leo *et al.*, 2019; Dietrich *et al.*, 2011; Vitousek *et al.*, 2017; Vousdoukas *et al.*, 2018;
62 Kirezci *et al.*, 2020; Almar *et al.*, 2021), and ship routing and design standards (Bitner-
63 Gregersen *et al.*, 2015; Bitner-Gregersen and Gramstad, 2018). Moreover, waves
64 influence the entire climate system due to their complex feedbacks with the atmosphere,
65 sea ice and the underlying ocean (Cavaleri *et al.*, 2012). For that matter, not only is the
66 monitoring of the present wave climate of paramount importance (Young, 1999; Caires
67 and Swail, 2004; Young *et al.*, 2011; Semedo *et al.*, 2008; 2011; 2014; Aarnes *et al.*,
68 2012; 2015), but also the accurate projection of global future wave conditions (Morim *et al.*,
69 2019, 2023; Lobeto *et al.*, 2021a,b).

70 Sea state observations are required to accurately describe the historical wave climate,
71 but long-term measurements are relatively limited. *In-situ* instruments, such as moored
72 buoys, have been used over the last five decades by many countries as part of their
73 operational observing capabilities. Some of these buoys can currently provide
74 approximately 45 years of (almost) continuous observations (Bidlot *et al.*, 2002). While
75 providing some of the most comprehensive wave datasets, often assumed as “ground
76 truth” (*e.g.*, Bidlot, 2020; Menendez, 2008; Semedo *et al.*, 2014), the most significant
77 disadvantage of *in-situ* observations is, nevertheless, their uneven global positioning,
78 found disproportionately near the coasts of industrialized countries, mainly in the
79 Northern Hemisphere (NH). In the absence of observations, wave modelling efforts like
80 reanalyses or hindcasts (*e.g.*, ERA5; Hersbach *et al.*, 2020; Bidlot *et al.*, 2019) provide
81 relatively accurate depictions of the global and local wave climates, being currently the
82 only available time- and space-continuous sources of a full spectral description of the
83 ocean surface. Despite the ever-greater accuracy of these modelling products, they rely
84 on forcing winds from atmospheric reanalyses, which often exhibit well-documented
85 biases and long-term inconsistencies (Ramon *et al.*, 2019; Torralba *et al.*, 2017). In fact,
86 despite the wave’s role in the climate system, no fully coupled ocean-wave-atmosphere
87 climate model exists yet, although some attempts have been conducted (*e.g.*, Lionello *et al.*
88 1998; Rutgersson *et al.* 2010).

89 Understanding the future evolution of the global wave climate poses one of the
90 greatest challenges in climate modelling. At the same time, it became an important issue
91 for decision and policy-makers in climate change adaptation and mitigation strategies
92 (Magnan *et al.*, 2016; Jones *et al.*, 2014). Future wave climate projections rely on wind
93 and sea ice simulations from global climate models (GCMs), used to force dynamic or
94 statistical wave models (Stopa *et al.*, 2019). Several studies exploring the impact of
95 climate change in future global wave climate have been conducted recently, using forcing
96 GCM outputs from the World Climate Research Program (WCRP) Coupled Model

97 Intercomparison Project phases 3 (CMIP3) and 5 (CMIP5), namely Mori *et al.* (2010),
98 Dobrynin *et al.* (2012), Fan *et al.* (2013), Hemer *et al.* (2013a), Semedo *et al.* (2013),
99 Wang *et al.* (2015), Dobrynin *et al.* (2015), Erikson *et al.* (2015), Kamranzad *et al.* (2015),
100 Hemer and Trenham (2016), Camus *et al.* (2017), Casas-Prat *et al.* (2018), Kamranzad
101 and Mori (2018), Morim *et al.* (2018, 2019), Kamranzad and Mori (2019) and Lemos *et al.*
102 *et al.* (2019, 2020a, 2020b, 2021a, 2021b) and Lobeto *et al.* (2021a, 2021b, 2022). While
103 the first studies were based on a single GCM forcing climate simulation (*e.g.*, Mori *et al.*,
104 2010; Hemer *et al.*, 2013a; Semedo *et al.*, 2013), the use of ensembles has been widely
105 adopted in more recent studies. The primary goal of the ensemble approach is to better
106 quantify the uncertainties associated with individual simulations (Hawkins and Sutton,
107 2009; Knutti and Sedlacek, 2010; Rauser *et al.*, 2015) for a more realistic depiction of the
108 variability, trends and extremes of past and future projected wave climates. These
109 uncertainties arise from various sources, namely the use of different GCMs, scenarios,
110 wave models, physical parameterizations, the inaccurate depiction of small-scale
111 processes not yet fully understood, or processes not resolved due to computational
112 constraints (Stocker *et al.*, 2013). Cascading uncertainties have often been a limiting factor
113 in climate studies, particularly at regional scales (Foley, 2010; Falloon *et al.*, 2014; Payne
114 *et al.*, 2015).

115 Most wave climate ensembles rely on a multi-forcing strategy, *i.e.*, different GCMs
116 were used to force dynamical or statistical wave model(s). Recently, Morim *et al.* (2019)
117 compiled the largest set (to date) of individual studies to quantify the uncertainties
118 associated with GCM wind forcing and emission scenarios. It was concluded that
119 uncertainty in current wave climate projections is mostly GCM-driven, in such a way that
120 considering multiple studies at once, robust projected changes in wave parameters (*i.e.*,
121 exceeding the natural historical variability) are only detectable for the RCP8.5 high
122 emissions scenario (Riahi *et al.*, 2011). This study, however, did not investigate to what
123 measure the use of different wave models and parameterizations while generating wave
124 climate projections impacts their uncertainty range and robustness. In fact, this relevant
125 uncertainty source has often been overlooked in the scientific literature (*e.g.*, Erikson *et al.*
126 *et al.*, 2015; Hemer and Trenham, 2016; Bricheno and Wolf, 2018; Morim *et al.*, 2019;
127 Lemos *et al.*, 2020b). Kumar *et al.* (2022), nevertheless, addressed it, in an attempt to
128 quantify the uncertainties in CMIP6 wave climate projections towards the end of the 21st
129 century using a 4-member ensemble, being the parameterizations (source terms; STs)
130 within the WaveWatchIII (WW3; Tolman *et al.*, 2009; WW3DG, 2019) wave model the
131 differentiating factor. Despite keeping the GCM forcing constant, it was concluded that
132 the uncertainties induced by different STs are enough to seriously affect the robustness
133 of the projections in several areas of the global ocean, even considering a high-emission
134 scenario (SSP5-8.5; O'Neill *et al.*, 2016).

135 To accurately quantify the impact of climate change, as the differences between the
136 future projected and historical climates, the ability of the ensemble to reproduce the
137 baseline (present) wave climate conditions (mean conditions, intra- and inter-annual
138 variabilities and extremes) must be previously evaluated. The accurate historical climate
139 representation is key to increasing user confidence in the associated future projections.
140 Therefore, a thorough evaluation of the ensemble's performance skills against long-term
141 historical observations or reanalyzes/hindcasts is required (*e.g.*, Semedo *et al.*, 2018b).

142 In the present study, a unique type of ensemble is presented and evaluated. In our
143 approach, a single CMIP6 GCM (EC-Earth3; Döscher *et al.*, 2022) is used to force seven
144 dynamic wave climate simulations. The differentiating factor between each ensemble

145 member (individual simulation) is the wave-model-parameterization pair used to generate
146 the wave climate simulations. In total, three different wave models are used: WW3,
147 SWAN (Booij *et al.*, 1996) and WAM (WAMDI Group, 1988) to produce seven different
148 simulations with multiple STs. The ensemble used here is therefore a “single forcing,
149 multi wave model” one, built to investigate the (usually discarded) impact of multiple
150 parameterizations on the wave climate (both historical and future projected ones). To do
151 so in an effective way, the remaining sources of uncertainty (*e.g.*, adopting a multi-forcing
152 strategies, different initializations, or even multiple future emission scenarios) were
153 limited. Near-surface wind speeds (U_{10}) and sea ice cover (SIC) are used as forcing for
154 the wave models (except SWAN, for which only U_{10} is required), both during the 1995-
155 2014 historical period (henceforth “PC20”) and 2081-2100 future projections (not
156 analyzed here). The PC20 ensemble is extensively evaluated through comparison with an
157 extensive *in-situ* observational set (buoys and platforms), and with the European Centre
158 for Medium-range Weather Forecasts (ECMWF) ERA5 reanalysis (Hersbach *et al.*,
159 2020). Our main goal is not to uniquely present a new ensemble of wave climate
160 simulations and projections, or to focus on an optimal output, but instead to assess the
161 uncertainty generated by an ensemble containing several wave models and
162 parameterizations, as in Morim *et al.* (2018, 2019). For the same reason, although quick
163 progress has been made to improve the overall quality of wave modelling results, we use
164 parameterizations that can be considered outdated, for example, ST1 (Komen *et al.*,
165 1994), ST2 (Tolman and Chalikov, 1996) and ST3 (Janssen, 2004; Bidlot *et al.*, 2007).
166 We aim to demonstrate to which extent there is a negative impact when pairing older
167 parameterizations with more recent ones in a single ensemble, in terms of uncertainty.

168 The remainder of the paper is structured as follows. In section 2, the EC-Earth3
169 GCM, the wave models, the reanalysis and the observational data are described, as well
170 as the general methodology for the evaluation process. In section 3, the performance skills
171 of the PC20 ensemble are assessed in depth, focusing on the representation of means,
172 extremes, short- and long-term variabilities and uncertainties along the historical time-
173 slice. A discussion of the obtained results, together with the concluding remarks, are
174 offered in section 4.

175 2. Data and methods

176

177 2.1. The EC-Earth3 GCM

178 The EC-Earth is a widely used GCM in both global and regional climate assessments,
179 collaboratively developed by the European Consortium (Döscher *et al.*, 2022). Here, the
180 CMIP6 generation of the model (EC-Earth3) is used, in version 3.3. The EC-Earth3 GCM
181 provides a description of the atmosphere (and its composition), ocean, sea ice, land
182 surface, dynamic vegetation, ocean biogeochemistry and Greenland ice sheet, using the
183 ECMWF Integrated Forecast System (IFS) model cycle CY36R4, coupled with the
184 Nucleus for European Modelling of the Ocean (NEMO) version 3.6, the sea ice model
185 LIM3 and the Pelagic Interactions Scheme for Carbon and Ecosystem Studies (PISCES)
186 biogeochemical model. Terrestrial parameters such as land use, dynamical vegetation and
187 biogeochemistry are given by the Lund-Potsdam-Jena General Ecosystem Simulator
188 (LPJ-GUESS). Additional details are available in Döscher *et al.* (2022).

189 In the context of CMIP5, the EC-Earth GCM was shown to provide one of the most
190 accurate representations of the historical U_{10} and SIC amongst its remaining counterparts
191 (Shu *et al.*, 2015; Casas-Prat *et al.*, 2018). More recently, within CMIP6, an evaluation
192 for wave climate modelling purposes conducted by Meucci *et al.* (2023) showed that EC-
193 Earth3 ranks as one of the best GCMs to represent sea level pressure and U_{10} values above
194 the global ocean. Nevertheless, positive U_{10} biases were still identified in the Northern
195 Hemisphere (NH) mid-latitudes, related to an equatorward storm track bias (Harvey *et al.*,
196 2020; Priestley *et al.*, 2020), and a relatively poor performance for SIC was detected
197 in the Southern Hemisphere (SH).

198 In this study, one realization of the EC-Earth3 was considered, the r1i1p1f1
199 (“realization” 1, “initialization” 1, “physics” 1, “forcing” 1) one, to force all the wave
200 climate simulations. This approach eliminates the uncertainty related to different forcings
201 on the GCM side, allowing the isolation of sources related to wave model physics and
202 parameterizations. The spatial domain ranges from 80.36°S to 80.64°N and 180°W to
203 179.296875°E in a 0.7° x 0.703125° (latitude x longitude) horizontal resolution grid for
204 all variables (U_{10} , defined by its longitudinal and meridional components uas and vas ,
205 and SIC, interpolated from a non-structured grid). The time resolution is 3 hours. The full
206 simulation period corresponds to 1984-2014 and 2070-2100, under the SSP5-8.5
207 scenario.

208 2.2. Wave models and parameterizations

209

210

2.2.1. *WW3*

211 The WW3 is a third-generation spectral wave model vastly used for operational wave
212 forecasting, research, and engineering applications. Here, WW3 version 6.07 (WW3DG,
213 2019) is used to generate four of the seven global wave climate simulations that compose
214 the ensemble. Within the model, physics and numerical schemes are defined by switches
215 (Tolman, 2009). The switches activated for the four WW3 runs considered here are as
216 follows:

- 217 • Third-order Ultimate Quickest (UQ) propagation scheme along with the
218 averaging technique (PR3) for garden sprinkler reduction (Tolman, 2002);

- 219 • Discrete interaction approximation (DIA; Hasselmann *et al.*, 1985) for
220 nonlinear wave-wave interactions (switch NL1);
- 221 • Linear input (switch LN1) from the parameterization of Cavaleri and
222 Malanotte-Rizzoli (1981), along with a low-frequency filter from Tolman
223 (1992), for consistent spin-up from calm conditions and improving initial
224 wave growth.
- 225 • Bottom friction (switch BT1) from the Joint North Sea Wave Project
226 (JONSWAP; Hasselmann *et al.*, 1973);
- 227 • Depth-induced wave breaking, accounted using the Battjes and Janssen
228 (1978) formulation (switch DB1);
- 229 • Miche-style shallow water limiter (switch MLIM) for maximum wave height;
- 230 • Deactivated reflections by shorelines and icebergs (switch REF0) and no
231 bottom or sea ice scattering (switches BS0 and IS0);
- 232 • Ice-blocking scheme (switch IC0) considering all grid-points with SIC over
233 50% as land.

234 Each of the four WW3 ensemble members correspond to a different input-dissipation
235 parameterization (ST package), namely the ST2 (Tolman and Chalikov, 1996), ST3
236 (Bidlot *et al.*, 2007 and Janssen, 2004; also named “BJA”), ST4 (Ardhuin *et al.*, 2010)
237 and ST6 (Zeiger *et al.*, 2015, Rogers *et al.*, 2012; Babanin, 2011). Generally, the default
238 parameter settings of each ST package are used. In ST4, coefficients corresponding to the
239 TEST471 option are selected, with $\beta_{max} = 1.43$, which generally provides the best results
240 at global scale (WW3DG, 2019). In ST6, switch FLX4 is activated using the air-sea
241 coupling factor CDFAC = 1. It should be highlighted that the ST6 parameterization in
242 WW3 v6.07 suffered a re-calibration, following Rogers *et al.* (2017) and Liu *et al.* (2019),
243 updating the U_{10} scaling factor to 32. Additional details can be found in Table SM1 in the
244 Supplementary Material and in Kumar *et al.* (2022).

245 The bathymetry is based on ETOPO-1 (Amante and Eakins, 2009) and the Global
246 Self-Consistent Hierarchical High-Resolution Shoreline (GSHHS) v1.10 Database. Three
247 files were created: bathymetry, mask, and obstruction grid accounting for wave
248 attenuation by unresolved islands, using the *gridgen* software package (Chawla and
249 Tolman 2007; 2008). The global output time step in WW3 was set to 3 hours, using a
250 spectral resolution of 29 frequencies, logarithmically ranging from 0.0350 Hz to 0.5047
251 Hz, and 24 directional bins of 15°. The domain and horizontal resolution of the wave
252 fields were kept the same as in the EC-Earth3 forcing winds. Bathymetry, time steps,
253 spectral characteristics, domain and resolution were kept the same for the remaining
254 ensemble members produced using the SWAN and WAM wave models, to limit
255 additional sources of uncertainty. The remaining model configurations were kept constant
256 whenever possible.

257 2.2.2. SWAN

258 The Simulating Waves Nearshore (SWAN; Booij *et al.*, 1999; Ris *et al.*, 1999) is a
259 third-generation spectral wave model used for several operational, research and
260 engineering applications. Here, the SWAN version 41.20AB is used to generate two of
261 the seven wave climate simulations. Similarly to the WW3 runs, each of the SWAN
262 members correspond to a different parameterization within the model, namely the ST1,
263 as the recommended SWAN default setting (SWAN Team, 2022) and ST6, with a degree
264 of equivalence to the WW3-ST6 (Donelan *et al.*, 2006; Rogers *et al.*, 2012). In fact,
265 although SWAN is more frequently employed to simulate waves across local to regional

266 domains, it shares most of the physical processes present in other models, as WW3 and
 267 WAM (Table SM1). Therefore, SWAN has been considered suitable to simulate waves
 268 at global scale (*e.g.*, Mori *et al.*, 2010; Liang *et al.*, 2019; Li and Zhang, 2020). Within
 269 the model, run in non-stationary model, general configurations are considered as follows:

- 270 • Garden sprinkler effect reduction according to Tolman (2002);
- 271 • DIA according to Hasselmann *et al.* (1985);
- 272 • Bottom friction formulation according to the JONSWAP (Hasselmann *et al.*,
 273 1973), but considering $C_{fjon} = 0.067 \text{ m}^2\text{s}^{-3}$ as in Zijlema *et al.* (2012);
- 274 • Depth-induced wave breaking as described in Battjes and Janssen (1978);
- 275 • Courant-type limiter, which deactivates quadruplets permanently when the
 276 Ursell number exceeds 10 (excluding cases when the fraction of breaking
 277 waves exceeds 1 under decreasing action density);
- 278 • Third-order upwind scheme according to Stelling and Leendertse (1992) with
 279 a diffusive correction for the garden sprinkler effect as in Booij and
 280 Holthuisen (1987).

281 In ST1, the wind and whitecapping formulations follow Komen *et al.* (1994) and
 282 Rogers *et al.* (2003). In ST6, some differences to the WW3-ST6 run should be
 283 highlighted, namely the inclusion of the new “SSWELL ARDHUIN” option for non-
 284 breaking dissipation from Ardhuin *et al.* (2010) as well as a U_{10} scaling factor of 28
 285 (Hwang, 2011). Additional details can be found in Table SM1.

286 2.2.3. WAM

287 The third-generation WAM wave model (WAMDI Group, 1988) version 4.6 is used
 288 to produce one of the seven wave climate simulations that compose the ensemble.
 289 Specifically, the default WAM settings of physical parametrizations from ECMWF
 290 CY45R1 (WAM Cycle 4.6.2.2; ECMWF, 2018) are considered, defined by the switch
 291 IPHYS = 0 (overall similar to the WW3-ST3 run), as follows:

- 292 • Wind input and wave growth according to Miles (1957) and Janssen (1991);
- 293 • DIA according to Hasselmann *et al.* (1985) and Komen *et al.* (1994);
- 294 • Bottom friction formulation as in Komen *et al.* (1994);
- 295 • Whitecapping dissipation according to Hasselmann (1974) and Janssen
 296 (1989a);
- 297 • Shallow-water mode.

298 This simulation, forced by the same 3-hourly EC-Earth3 winds and daily SIC as
 299 previous ensemble members, also preserves all remaining setup characteristics, including
 300 bathymetry (despite previously converted into a WAM format regular grid), time steps
 301 and spectral resolution. Additional details can be found in Table SM1.

302 2.3. The ERA5 reanalysis

303 The ERA5 reanalysis provides a comprehensive, high-resolution record of the global
 304 atmosphere, land surface, and ocean wind waves from 1950 onwards, continuing to be
 305 extended in almost real-time. It is produced using the IFS cycle CY41R2 (ECMWF,
 306 2016), used for the operational forecast from March to November 2016. ERA5 uses an
 307 advanced data assimilation system (4D-Var scheme). The horizontal resolution of the
 308 atmospheric model in ERA5 is about 30 km ($0.25^\circ \times 0.25^\circ$), being the resolution of the
 309 wave parameters approximately 40 km ($0.36^\circ \times 0.36^\circ$). The time resolution is 1 hour. The
 310 wave component in ERA5 is produced with a specific configuration of the WAM model

311 named as “ECWAM”, based on WAM Cycle 4 (Bidlot, 2007), yet providing a better
312 representation of long-period swells and dissipation levels due to white-capping, as
313 described in Bidlot et al. (2012). Extra output parameters were also introduced to better
314 characterize freak waves, based on the work from Janssen and Bidlot (2009). ERA5 wave
315 spectral domain ranges for 30 logarithmically spaced frequency bins, from 0.03453 Hz to
316 0.5478 Hz, and 24 directional bins of 15°. The bathymetry in ERA5 is based on the
317 ETOPO2 (NGDC, 2006) dataset. Altimeter wave height wave has been assimilated by
318 the wave model component of the system. Additional details regarding the ERA5
319 reanalysis can be found in Hersbach *et al.* (2020). Here, the ERA5 is used upon
320 interpolation into the wave climate simulations’ grid.

321 2.4. *In-situ* data

322 An extensive *in-situ* observational dataset (from buoy and oil platform observations)
323 is used to complement the ensemble performance evaluation. The original ECMWF *in-*
324 *situ* observational data set, obtained via the WMO Global Telecommunication System
325 (GTS), has regularly been used to evaluate the operational wave forecasts (Bidlot *et al.*,
326 2002, 2007; Bidlot, 2017), was complemented with *in-situ* wave and wind measurements
327 from Australia, Portugal (mainland and Azores), Baltic Sea and Brazil. The *in-situ*
328 observations from Australia were supplied by Australia’s Integrated Marine Observing
329 System (IMOS; enabled by the National Collaborative Research Infrastructure Strategy
330 – NCRIS). The *in-situ* data from Portugal mainland and the Azores were supplied by the
331 Portuguese Hydrographic Institute and by the CLIMAAT (Portuguese acronym, as Clima
332 e Meteorologia dos Arquipélagos Atlânticos) project, respectively. On the other hand, the
333 observations from the Baltic Sea were supplied by the CMEMS (Copernicus Marine
334 Environment Monitoring Service) and the BOOS (Baltic Operational Oceanographic
335 System) online platforms, and the *in-situ* data from Brazil were obtained from the
336 PNBOIA (Portuguese acronym, as Programa Nacional de Bóias).

337 A quality control assessment was performed for all *in-situ* observations. From the
338 raw dataset, in the first stage, only the *in-situ* instruments with unchanged geographical
339 positioning by more than 1° latitude or longitude from their nominal locations were
340 selected. If this limit was exceeded during a short time (random errors), nevertheless, the
341 observations outside the interval were still considered valid. If the geographical position
342 changed consistently to a different location, observations were still considered valid, yet
343 separately for both locations. All *in-situ* measuring instruments with a reported significant
344 wave height resolution above 0.1 m, a mean or peak wave period resolution above 1 s,
345 and a wind speed resolution above 1 m/s, were automatically excluded. Finally, *in-situ*
346 locations with less than 10 years of measurements or more than 30% of invalid data were
347 removed from the analysis. Upon the selection process, a total of 260 (194) *in-situ*
348 locations remained for the significant wave height (peak wave period) parameter. Their
349 geographical distribution is shown in Fig. 1.

350 2.5. Methodology

351 The ensemble in the present study is composed of seven members, being the
352 differentiating factor the wave model and/or the physics parameterization (ST) used to
353 generate each wave climate simulation. All spatial and temporal resolutions between the
354 forcing fields and final outputs are the same. Other inputs, such as bathymetry and land
355 mask, were also preserved between ensemble members, even when considering different
356 wave models. Here, we aimed to restrict the ensemble uncertainty sources (the “degrees
357 of freedom”) to represent only the impact of varying wave model architectures and STs.

358 All the remaining sources, better illustrated in Morim *et al.* (2019), are kept constant to
 359 the maximum possible extent.

360 A set of four wave parameters is analyzed, comprising long-term climate simulations
 361 of significant wave height (H_S), mean energy wave period ($T_{m-1,0}$ or simply T_m), peak
 362 wave period (T_p) and mean wave direction (MWD). The ensemble mean considers a
 363 democratic approach: the unweighted mean of the seven ensemble members (as in
 364 Semedo *et al.*, 2018b; Lemos *et al.*, 2019; 2020a; 2020b; 2021a; 2021b; Kumar *et al.*,
 365 2022). For convenience, when referring to individual ensemble members, the notation
 366 PC20- i (where $i = 1$ to 7) is used. The first four members ($i = 1$ to $i = 4$) correspond to the
 367 WW3 wave climate simulations under ST2, ST3, ST4 and ST6 parameterizations,
 368 respectively. The remaining members ($i = 5$ to $i = 7$) refer to the SWAN (ST1 and ST6)
 369 and WAM simulations, respectively. The 3-hourly wind and wave parameters were
 370 processed for both an annual and seasonal (December to February – DJF and June to
 371 August – JJA) analysis.

372 The performance evaluation is carried out at both global and regional scales,
 373 considering 13 different sub-areas, chosen according to Alves (2006). These are detailed
 374 in Fig. 1 and Table SM2. The evaluation metrics considered here include the Bias (Eq.
 375 1), the normalized bias (NBias; Eq. 2), the root mean squared error (RMSE; Eq. 3), the
 376 correlation coefficient (R; Eq. 4), the normalized RMSE, or scatter index (SI; Eq. 5), the
 377 slope associated with the linear regression between simulated and reference fields (SL),
 378 and the non-dimensional arcsin–Mielke score, or M-score (Watterson, 1996; Watterson
 379 *et al.*, 2014; Semedo *et al.*, 2018b; Lemos *et al.*, 2020a; Eq. 6), the mean annual variability
 380 index (MAV; Stopa *et al.*, 2014; 2018; Eq. 7) and the inter-annual variability index (IAV;
 381 Stopa *et al.*, 2018; Lemos *et al.*, 2019; Eq. 8).

$$\text{Bias} = \overline{\text{PC20}} - \overline{\text{REF}} \quad (1)$$

$$\text{NBias} = \frac{\overline{\text{PC20}} - \overline{\text{REF}}}{\overline{\text{REF}}} * 100\% \quad (2)$$

$$\text{RMSE} = \sqrt{\frac{\sum_{i=1}^N (\text{PC20}_i - \text{REF}_i)^2}{N}} \quad (3)$$

$$r = \frac{\sum_{i=1}^N (\text{REF}_i - \overline{\text{REF}})(\text{PC20}_i - \overline{\text{PC20}})}{\sqrt{\sum_{i=1}^N (\text{REF}_i - \overline{\text{REF}})^2} \sqrt{\sum_{i=1}^N (\text{PC20}_i - \overline{\text{PC20}})^2}} \quad (4)$$

$$SI = \frac{\sqrt{\frac{\sum_{i=1}^N (PC20_i - REF_i)^2}{N}}}{REF} \quad (5)$$

$$M = \frac{2}{\pi} \arcsin \left(1 - \frac{MSE}{V_{PC20} + V_{REF} + (G_{PC20} + G_{REF})^2} \right) * 1000 \quad (6)$$

$$MAV = \frac{1}{Y} \frac{\sum_{j=1}^Y \sqrt{\frac{1}{N} \sum_{i=1}^N \left(X_{ji} - \left(\frac{1}{N} \sum_{i=1}^N X_{ji} \right) \right)^2}}{\frac{1}{N} \sum_{i=1}^N X_{ji}} = \left(\frac{\sigma_X}{\bar{X}} \right) \quad (7)$$

$$IAV = MAV, \text{ but considering an inter-annual scale (i.e., excluding } i) \quad (8)$$

382 In Eqs. (1) to (8), PC20 refers to the wave climate simulations, REF to the reference
 383 data (ERA5 reanalysis or *in-situ* observations), and X to situations where both are used.
 384 Throughout the formulas, N corresponds to the number of outputs considered. In Eq. (6),
 385 MSE is the mean squared error, V the spatial variance and G the spatial mean. The M-
 386 score performance measure ranges from a hypothetical zero for no skill (MSE = ∞), to a
 387 hypothetical maximum score of 1000 (MSE = 0). In Eqs. (3-5) and (7-8), i corresponds to
 388 the data index, here as multi-year daily means, computed prior to the evaluation process,
 389 in order to avoid the constraints of non-synchrony between the wave climate simulations
 390 and the reference data. In Eq. (7), j corresponds to the Julian year's index, being Y the
 391 total number of Julian years considered (here set as 20). The MAV (IAV) corresponds to
 392 the average of the intra-annual (inter-annual) standard deviation normalized by the yearly
 393 (full) mean, providing an indication of the dataset's spread and ability to simulate
 394 extremes.

395 For the comparison between PC20, ERA5 and *in-situ* observations, all multi-year
 396 daily averages were collocated through bilinear interpolation to the *in-situ* locations. In
 397 the higher latitudes, SIC extent variability can dramatically affect the quality of the mean
 398 wave fields, due to a considerable reduction of the available outputs at each grid-point
 399 (considered as land when SIC exceeds 50%). Therefore, here, possible inadequate
 400 sampling issues at the higher latitudes were dealt with by using one of the approaches
 401 proposed by Tuomi *et al.* (2011): grid-points coded as land during 30% or more of the
 402 analyzed period were ruled out of the statistics, leaving only the remaining grid-points to
 403 be treated as open water.

404

3. Results

405 The normalized biases (in %) between the annual, DJF and JJA EC-Earth3 and ERA5
 406 mean U_{10} values are shown in Fig. 2. At an annual scale (corresponding to the entire
 407 1995-2014 period; Fig. 2a), the EC-Earth3 performs better in the extratropical areas than
 408 in the tropical, where mostly underestimations are visible, surpassing -20% in the Atlantic
 409 region between Brazil and the Gulf of Guinea, and in the tropical North Pacific, south of
 410 Hawaii. Local overestimations of up to 20% are visible near the Maritime Continent. In
 411 the remaining areas of the global ocean, normalized biases are generally low, below 12%.
 412 It should be noted that differences are even lower throughout the Southern Ocean (the
 413 single largest global wave generation area), ranging mostly between -4% and 4%. During
 414 DJF (Fig. 2b), the patterns are similar to the ones in Fig. 2a, with exacerbated differences
 415 in the tropical areas, ranging between -52% and 28% in the Atlantic, -36% and 44% in
 416 the Pacific and -20% and 28% in the Indian basins. These are essentially related to the
 417 positioning of the Intertropical Convergence Zone (ITCZ) in EC-Earth3, showing a
 418 slightly positive latitudinal displacement during DJF, when compared to ERA5. In JJA
 419 (Fig. 2c), normalized biases are usually higher, above 4% in most of the global ocean.
 420 During this season, while some of the greatest differences are still visible along the
 421 tropical areas (mostly negative, down to -36%), positive ones are detectable in the higher
 422 latitudes of both hemispheres (up to 36% in the SH and 44% in the NH). Such behavior
 423 might be related to a worse representation of the polar vortexes by EC-Earth3 during JJA
 424 (Döscher *et al.*, 2022). Nevertheless, Fig. 2 demonstrates that the EC-Earth3 is able to
 425 represent the near-surface wind speeds at a global scale with relatively high accuracy. It
 426 should be noted that the modelling frameworks of EC-Earth3 and ERA5 are relatively
 427 similar (*e.g.*, both using IFS), which could contribute to an enhanced performance against
 428 this reanalysis. Overall, EC-Earth3 is considered appropriate to provide forcing to the
 429 seven wave climate simulations.

430 Fig. 3 shows the annual mean (left) and 95% percentile (right) H_S normalized biases
 431 between each member of the PC20 ensemble and ERA5. Ensemble members are ordered
 432 vertically from PC20-1 to PC20-7. Substantial differences between each member are
 433 visible, in both the representation of the annual mean H_S values, and the extremes.
 434 Normalized biases range from mostly negative at a global scale (PC20-1 – WW3-ST2
 435 and -6 – SWAN-ST6, in Figs. 3a,b,k,l), to mostly positive (PC20-5 – SWAN-ST1 and -7
 436 – WAM4.6, in Figs. 3i,j,m,n, but also visible for the extreme H_S values for the PC20-2 –
 437 WW3-ST3, in Fig. 3d). For the H_S annual mean, the WW3-ST4 (PC20-3) corresponds to
 438 the model-parameterization pair that yields overall lower global biases, averaging at
 439 0.98% (Table SM3) and not exceeding 20% (Fig. 3e). For the 95% percentile H_S , PC20-
 440 4 (WW3-ST6) shows the best performance, with differences averaging globally at 0.27%
 441 (Fig. 3h and Table SM3). Interestingly, the opposite is visible for the SWAN-ST6 pair,
 442 averaging at -25.2% and -20.1%, respectively. The impact of model parameterizations in
 443 the accuracy of swell propagation is clearly noticeable: for PC20-5 (SWAN-ST1) and -7
 444 (WAM4.6), the highest (positive) normalized biases are found in the tropical latitudes,
 445 with lower values in the extratropics, revealing an overestimation of long swell energy
 446 content. For PC20-1 (WW3-ST2) and -6 (SWAN-ST6) a similar pattern is observed,
 447 however in a global underestimation. Throughout the WW3 simulations (PC20-1 to -4),
 448 the agreement between each member and ERA5 tends to increase. This feature highlights
 449 the latest efforts in creating ever-more accurate wave model parameterizations, such as
 450 the ST4, with an improved swell attenuation scheme (Ardhuin *et al.*, 2010), and ST6,
 451 containing both physical and observation-based source terms (Liu *et al.*, 2019; 2021).
 452 Note that the widespread H_S underestimation in PC20-1 (WW3-ST2; Fig. 3a,b) is related

453 to a known overestimation of swell dissipation in ST2 which, as a result, underestimates
 454 deep-ocean wave growth under stable atmospheric conditions (Tolman, 2002). On the
 455 other hand, the overestimations visible for PC20-2 (WW3-ST3; Fig. 3c,d) are mainly
 456 related to dissipation constrains depending on swell height, influencing dissipation at the
 457 wind-sea peak. Note that, while similar to the WAM4 parameterization (here represented
 458 in PC20-7, WAM4.6), the WW3-ST3 run with “BJA” dissipation terms shows a generally
 459 better performance than the former, a result which is also described in the WW3 v6.07
 460 manual (WW3DG, 2019).

461 An optimal balance between the correct description of energy input from the
 462 overlaying winds at the wave generation areas, its conversion into swell, and the correct
 463 dissipation upon propagation, is not yet obtained, as it is visible in Fig. 3. Even for the
 464 WW3-ST4 pair (PC20-3; Figs. 3e,f), with better global performance, slightly positive
 465 (negative) biases are visible in the extratropical (tropical) latitudes. Such differences
 466 reveal that inaccuracies may still be present in processes such as swell attenuation (wave
 467 growth and dissipation due to white-capping) mostly in the low (mid-to-high) latitudes,
 468 in comparison with ERA5. Note that ERA5 presented a very reasonable H_S agreement
 469 with observations in tropical areas, as it was shown in Bidlot *et al.* (2019). For DJF and
 470 JJA mean and 95% percentile H_S (Figs. SM1 and SM2 in the Supplementary Material –
 471 SM), despite an expected seasonal shift in the main and extreme patterns from each
 472 ensemble member, the overall bias behavior remains similar. Therefore, it is only fair to
 473 assume that the main features shown in Fig. 3 are preserved throughout the year.

474 Fig. 4 is similar to Fig. 3, but for the T_m parameter. As shown for H_S , ensemble
 475 member performance varies considerably depending on the model-parameterization pair.
 476 Although, in general, a slight overestimation of the mean and extreme (95% percentile)
 477 T_m values is visible, mostly below 28%, for PC20-1 (WW3-ST2) and -6 (SWAN-ST6) a
 478 widespread underestimation occurs, especially along the subtropics (down to -20%).
 479 Among the seven ensemble members, PC20-4 (WW3-ST6) shows the best agreement
 480 with ERA5, globally differing, on average, 0.83% (2.11%) considering the mean (95%
 481 percentile) T_m (Table SM4). Seasonally, while the normalized bias patterns are similar to
 482 the annual ones during DJF (despite slightly higher values in the tropical areas, as visible
 483 in Fig. SM3 in the SM), during JJA (Fig. SM4 in the SM), differences are especially
 484 relevant in the NH. In fact, during the Austral winter (JJA), the increase in wave
 485 storminess in the Southern Ocean (Lobeto *et al.*, 2022) allows for the generation of longer
 486 and more energetic swells that deflect to the left (due to the Coriolis force) and propagate
 487 northwards, easily surpassing the equator line (Lemos *et al.*, 2021b). Accurate modelling
 488 of swell attenuation rates is especially challenging, and therefore, for most ensemble
 489 members, normalized biases attain higher values at longer-swell-arriving locations during
 490 JJA.

491 Fig. 5 depicts the annual mean MWD absolute biases (in °) between each PC20
 492 ensemble member and ERA5. MWD means are obtained following the appropriate
 493 formula for directional means, *i.e.*, by computing the arctangent of the quotient between
 494 components. Each member from PC20-1 to -7 is presented sequentially (Fig. 5a-g). MWD
 495 biases are usually higher in high intra-annual variability areas, such as in the subtropics,
 496 where a clear influence of the ITCZ positioning is visible, and along near-polar areas, but
 497 especially in the NH, possibly due to a more challenging representation of SIC variations.
 498 For PC20-5 (SWAN-ST1; Fig. 5e) and -7 (WAM4.6; Fig. 5g), the enhanced swell
 499 propagation from the Southern Ocean compared to ERA5 (also revealed by the
 500 overestimations found for H_S and T_m in Figs. 3 and 4) is visible through large areas of

501 positive (clockwise) biases, especially in the central Pacific (Table SM5). For the
 502 remaining ensemble members, the overall agreement is good, with differences below 36°
 503 in most of the global ocean. Along the extratropical latitudes of both hemispheres, biases
 504 below 12° are dominant. The seasonal behavior of the *MWD* biases (in Figs. SM5 and
 505 SM6 of the SM for DJF and JJA, respectively) is strongly related to seasonal atmospheric
 506 phenomena, such as the main position of the main atmospheric synoptic circulation
 507 systems, ITCZ, and the aforementioned swell propagation issues. Higher seasonal biases
 508 are dominant in the SH during DJF (except for PC20-5 and -6) and in the NH during JJA.
 509 Seasonal biases remain relatively low in most of the global ocean, nevertheless.

510 Figs. 6 and 7 show the (left) H_S and (right) T_p merged scatter-QQ-plots and the intra-
 511 annual cycles, respectively, for the performance evaluation between PC20-1 to -7 and the
 512 reference datasets, here exclusively at the *in-situ* locations. It should be noted that until
 513 recently, the WMO GTS data only reported H_S and T_p for most *in-situ* locations.
 514 Therefore, the majority of the wave period observations in the dataset correspond to T_p
 515 instead of T_m . To avoid the effects of the non-synchronized climates between model
 516 simulations and reference datasets, multi-year annual means were considered in both
 517 figures, and only *in-situ* locations with at least 10 years of continuous observations were
 518 selected. The global ocean is divided into areas to evaluate regional performance. Only
 519 areas with at least 10 *in-situ* locations available were selected. TWSP and ETSP are
 520 shown together to enhance the robustness of the results, given the low number of locations
 521 available for ETSP.

522 Across the ETNA area, 89 (24) locations were selected for H_S (T_p). At these
 523 locations, Fig. 6a shows compatible results to those in Fig. 3: while PC20-1 (WW3-ST2)
 524 and -6 (SWAN-ST6) show a consistent H_S underestimation, with mean biases of -0.29 m
 525 and -0.27 m, respectively, PC20-5 (SWAN-ST1) and -7 (WAM4.6) show the greatest
 526 overestimations, with mean biases of 0.41 m and 0.37 m (Table 1). Biases for the 99%
 527 percentile range from -0.80 m (PC20-6) to 0.64 m (PC20-7). Such features are noticeable
 528 throughout the entire year, as shown in Fig. 7a. Nevertheless, differences attain greater
 529 values during the boreal winter season, when the uncertainty range between ensemble
 530 members exceeds 1 m. Table 2 shows that, for some members, the performance of
 531 extreme H_S is better than the average. In fact, for PC20-2, -3 and -5, biases tend to
 532 decrease above the 90% percentile. Nevertheless, the best overall agreement is found for
 533 the PC20-3 (WW3-ST4) and -6 members (as in Fig. 3), with mean (extreme) biases of
 534 0.12 m and -0.02 m (0.01 m and -0.09 m). The remaining metrics show relatively similar
 535 values for all model-parameterization pairs, with RMSEs, Rs and SIs ranging between
 536 0.46 m (PC20-3) and 0.60 m (PC20-7), 0.87 (PC20-1) and 0.88 (PC20-7) and 0.24 (PC20-
 537 3) and 0.32 (PC20-7). In terms of T_p (Fig. 6b), PC20-1 and -6 show consistent
 538 underestimations, averaging at -1.01 s and -0.31 s, respectively (Table 3). The greatest
 539 overestimations are visible for PC20-5, -7 and -2, at 1.49 s, 0.78 s and 0.47 s on average,
 540 respectively. For these members, biases for the 99% percentile onwards surpass 2 s (Table
 541 4). Throughout the year, T_p differences are greater during the boreal summer season,
 542 when the inter-member uncertainty range exceeds 3 s (mostly due to the PC20-2 and -5
 543 members; Fig. 7a). Similarly to H_S , PC20-3 and -4 (WW3-ST6) show the best agreement
 544 with *in-situ* observations, with mean (extreme) biases of 0.11 s and 0.06 s (below 1.4 s).
 545 Overall, RMSEs and SIs range from 0.95 s and 0.12 (PC20-3) to 1.83 s and 0.22 (PC20-
 546 5), being the R values generally lower than for H_S .

547 For the TNAO area, a set of 42 (39) *in-situ* locations were used to locally evaluate
 548 H_S (T_p). In Fig. 6c, it can be seen that H_S is mostly underestimated at these locations, with

549 only PC20-5 (SWAN-ST1) and -7 (WAM4.6) showing a consistent overestimation
 550 (Table 1), nevertheless, starting from the 30% percentile (Table 3). Note that across
 551 TNAO, ERA5 also shows a slight underestimation compared to observations and
 552 therefore, while PC20-2 (WW3-ST3) and -3 (WW3-ST4) biases are very close to zero
 553 compared to the reanalysis, deviations assume greater values facing the *in-situ*
 554 observations (-0.07 m and -0.04 m, respectively; Table 1). However, overall, the bias
 555 range (also a proxy to the overall ensemble uncertainty range) is tighter compared to
 556 ETNA, from -0.36 m (-0.46 m) to 0.09 m (0.54 m) for the mean (95% percentile) H_S
 557 (Tables 1 and 2). Throughout the year, while PC20-1 (WW3-ST2), -4 (WW3-ST6) and -6
 558 (SWAN-ST6) show consistent underestimations, more evident during the boreal summer
 559 (between -0.2 m and -0.3 m), the remaining members' performance varies between
 560 extreme seasons, being most differences positive (negative) during the boreal winter
 561 (summer), as visible in Fig. 7c. At TNAO, H_S RMSEs, Rs and SIs vary between 0.34 m
 562 and 0.50 m, 0.79 and 0.83 and 0.27 and 0.39, respectively. For T_p , Fig. 6d shows a more
 563 consistent representation between ensemble members, with mean biases between -0.17 s
 564 and 0.24 s, apart from PC20-1 (-0.97 s) and -6 (-1.02 s; Table 3). Deviation patterns are
 565 also relatively constant throughout the year (Fig. 7d). RMSEs, Rs and SIs range between
 566 1.02 s and 1.55 s, 0.75 and 0.84 and 0.14 and 0.21.

567 At ETNP, 84 (79) *in-situ* locations matched the required criteria for H_S (T_p). The
 568 performance of individual ensemble members in this area varies considerably, even
 569 within each model-parameterization pair. While the H_S performance in Fig. 6e is similar
 570 to ETNA's one (Fig. 6a), at ETNP the bias range is greater and inter-member uncertainty
 571 is dominated by the SWAN simulations, from -0.38 m (PC20-6; SWAN-ST6) to 0.70 m
 572 (PC20-5; SWAN-ST1) for the mean H_S (Table 1). For PC20-5 and -7 (WAM4.6),
 573 differences peak between the 10% and the 50% percentiles (Table 2). R coefficients peak
 574 for the WW3 simulations, at 0.91, the highest value found for all analyzed areas. RMSEs
 575 vary between 0.38 m and 0.78 m and SIs between 0.19 and 0.38. Within the average year,
 576 in Fig. 7e, the behavior of the ensemble members is relatively consistent, despite a slight
 577 best (worst) performance for PC20-2 and -3 (PC20-5) during the boreal summer. T_p
 578 values are generally higher across ETNP than in the remaining areas of the global ocean,
 579 partially due to the arrival of long swells generated in the Southern Ocean (Fig. 6f).
 580 Nevertheless, most ensemble members reveal a consistent overestimation (except PC20-
 581 1; Tables 3 and 4), up to 2.85 s for the mean T_p (PC20-5). R values are slightly lower than
 582 for H_S , within 0.68–0.86. RMSEs and SIs range between 1.18 m and 3.37 m, and 0.11
 583 and 0.31, respectively. The mean yearly cycles in Fig. 7f show that, at ETNP, most
 584 ensemble members perform worse during summer. In fact, while the mean observed T_p
 585 is close to 10 s from May to September, overestimations of up to 4 s (~40%) are visible
 586 during this period.

587 Across the TWSP / ETSP areas, 22 (29) *in-situ* locations were selected for H_S (T_p).
 588 Fig. 6g shows that H_S is mostly overestimated by the ensemble members, with only a very
 589 slight underestimation (on average) by PC20-1 (WW3-ST2), of -0.02 m (Table 1). This
 590 is, in fact, the best performing model-parameterization pair at these areas. The remaining
 591 (positive) biases for the mean H_S reach 0.63 m (PC20-7; WAM4.6). For the extreme H_S ,
 592 nevertheless, both PC20-1 and -6 (SWAN-ST6) show underestimations, down to -0.70 m
 593 (Table 2). RMSEs, Rs and SIs range within 0.43–0.67 m, 0.76–0.82 and 0.35–0.57
 594 (highest obtained values), respectively. The generalized H_S overestimation is visible
 595 throughout the year, especially for PC20-5 (SWAN-ST1) and -7 (WAM4.6). Ensemble
 596 performance (inter-member uncertainty range) is slightly better (lower) during the austral

597 winter (Fig. 7g). In terms of T_p (Fig. 6h), mean biases vary between -1.09 s and 1.90 s for
 598 PC20-1 and -5, respectively (Table 3). Extreme differences are usually below 2 s (Table
 599 4). The remaining metrics show T_p performance to be slightly better than the H_S one, with
 600 Rs ranging between 0.75 s and 0.88 s and SIs between 0.11 and 0.24. RMSEs vary within
 601 1.26–2.17 s. Similar to H_S , Fig. 7h shows that along the average year, T_p biases and inter-
 602 member uncertainty are reduced during the austral winter in TWSP / ETSP.

603 Fig. 8 displays the average intra-annual H_S cycles for each of the 13 regional areas,
 604 considering all grid-points available across each one, for both the PC20 ensemble
 605 members, and ERA5. At ETNA, TNAO and ETNP, results are somewhat similar to those
 606 of Fig. 7. Yet, at ETNA (Fig. 8a), most members show a slight underestimation *versus*
 607 ERA5, and at ETNP (Fig. 8b), the performance of PC20-5 (SWAN-ST1) and -7
 608 (WAM4.6) is considerably better than in Fig. 7e. While the intra-annual H_S cycles are
 609 generally well represented by all ensemble members, the agreement with ERA5 is
 610 maximized at the extratropical areas of the NH (Figs 8a,b). At ETSA, ETSP and ETSI
 611 (Figs. 8c,d,e), PC20-1 (WW3-ST2) and -6 (SWAN-ST6) show a worse, isolated
 612 performance, considerably increasing inter-member uncertainty. In fact, in these areas (as
 613 well as in TENP and TESP), parameterization-driven uncertainty ranges consistently
 614 between 1 m and 1.5 m. Fig. 9 is similar to Fig. 8, but for T_m . For this parameter,
 615 performance is more consistent between areas, with an overall underestimation by PC20-
 616 1 and -6, and overestimation by PC20-5, -7, and often -2. Inter-member uncertainty varies
 617 between 2 s and 3 s. Complementarily, the evolution of the global and regional monthly
 618 H_S and T_m means during the historical 1995-2014 period is shown in Figs. SM7 and SM8
 619 in the SM. At a global scale (Figs. SM7n and SM8n), the differences between members
 620 and ERA5 are similar to the regionally described in Figs. 8 and 9. No major trends are
 621 identifiable during this period for both the PC20 simulations and ERA5.

622 Fig. 10 presents the H_S MAV (Eq. 7) normalized differences (in %), between each
 623 PC20 ensemble member and ERA5. It is noticeable that most model-parameterization
 624 pairs tend to overestimate intra-annual variability, especially in the tropical and
 625 subtropical areas of the NH (mostly below 18%), potentially due the combined
 626 misrepresentation of local tropical phenomena (such as the positioning and strength of
 627 the ITCZ; Fig. 2) and the highly seasonal mid-latitude storm belt. An exception is PC20-
 628 5 (SWAN-ST1; Fig. 10e) and partially PC20-7 (WAM4.6; Fig. 10g), for which a slight
 629 but generalized variability underestimation is visible. PC20 MAVs show a better
 630 agreement with ERA5 across the SH, with differences generally below 6%, especially in
 631 the Southern Ocean, possibly due to lower seasonal variability resulting from the almost
 632 permanent zonal winds. While results are similar for T_m (Fig. SM9 in the SM), MAV
 633 differences for this parameter are more circumscribed to the tropical areas.

634 Fig. 11 is similar to Fig. 10, but for the differences between the H_S IAVs (in %).
 635 While most ensemble members showed an overestimation of the MAVs, in this case,
 636 slight underestimations are dominant, mainly between -0.5% and -3.5%. Most ensemble
 637 members depict areas of positive differences, however, in regions dominated by tropical
 638 cyclone activity, namely across the western tropical Pacific and in the Gulf of Mexico.
 639 H_S IAVs also tend to diverge in the higher latitudes, possibly due to long-term differences
 640 in sea ice area extent between EC-Earth3 and ERA5 (except for the PC20-7 and PC20-6;
 641 Figs. 11e,f). Considering T_m (Fig. SM10 in the SM), differences are generally of lower
 642 magnitude, however, following similar overall patterns as for H_S .

643 The boxplots of the ensemble members' H_S and T_m M-scores (Eq. 6), computed for
644 the global ocean and for each of the 13 regional areas, are shown in Fig. 12, considering
645 the annual (grey), DJF (blue) and JJA (red) mean fields. The highest mean H_S M-scores,
646 generally with the lowest uncertainty ranges between model-parameterization pairs, are
647 visible for the extratropical latitudes of both hemispheres, peaking at ETNA (annually
648 and during DJF) and ETSP (during JJA; Fig. 12a). Between members, the highest (lowest)
649 extratropical annual M-score is obtained for the ETNP (ETSP) area at 928 (511).
650 Seasonally, ETNP (ETSI) presents the highest (lowest) M-score, at 895 (509) during DJF,
651 whereas ETSP presents both during JJA, from 464 to 908 (Table SM6). Interestingly,
652 extreme seasonal M-scores are found in the same hemisphere or even in the same area,
653 highlighting the potential differences induced by model-parameterization pairs in the
654 description of the seasonal H_S climate. Overall, the lowest extratropical scores are
655 obtained for the PC20-6 (SWAN-ST6), and the highest occur for the PC20-4/2 (WW3-
656 ST4/ST2) members. Across the tropical areas, H_S M-scores are generally lower,
657 especially at TWSP during JJA, ranging between 119 (PC20-5; SWAN-ST1) and 571
658 (WW3-ST3). The remaining tropical areas show H_S M-scores between 198 and 952
659 (Table SM6). For T_m , the regional behavior differs: while lower scores are generally
660 observable for some of the tropical areas (TSAO, TENP and TESP; Fig. 12b), others show
661 performances comparable to the extratropical latitudes (TNAO, TWNP, TWSP, TNIO
662 and TSIO). On the other hand, ETSP and ETSI show only reasonable overall T_m M-
663 scores, mostly between 400 and 700 (Table SM7). At a global scale, nevertheless, both
664 H_S and T_m show a good agreement with ERA5, with M-scores between 713 and 940, and
665 618 and 911, respectively. Between ensemble members, scores are consistently higher for
666 PC20-2 to 4 (WW3-ST3, -ST4 and -ST6).

667

4. Discussion and conclusions

668 In this paper, a performance evaluation was conducted for a 7-member CMIP6
669 single-forcing, multi-model ensemble of wave climate simulations. The ensemble was
670 built using three different wave models, to investigate the influence of different model-
671 parameterization pairs on the description of the present global wave climate, and on the
672 future projections towards the end of the 21st century (not shown). This uncertainty source
673 is often overlooked in wave climate studies using large, multi-model ensembles, and an
674 accurate quantification of its impacts on the overall ensemble spreads had not yet been
675 conducted. Large uncertainty ranges within ensembles are one major constraint in the
676 correct attribution of future climate change signals (Wallace *et al.*, 2015; Dobrynin *et al.*,
677 2015). Here, we aimed to characterize the ensemble performance in representing the
678 global and regional wave climates, using the ERA5 reanalysis and an extended, quality-
679 controlled set of *in-situ* observations as references to conduct the analysis.
680 Simultaneously, we focused on the model-parameterization-induced spreads within the
681 ensemble. Note that the 7-member ensemble used in this study contains several
682 parameterizations that could be considered outdated by the present-day wave modelling
683 standards. These were purposely included to account for the uncertainty generated by an
684 ensemble containing multiple model-parameterization configurations, even outdated
685 ones, as in Morim *et al.* (2018, 2019).

686 Regarding the forcing EC-Earth3 wind speeds, it was shown in Fig. 2 that the greatest
687 differences are located in the equatorial areas at the annual and seasonal (DJF) scales.
688 During JJA, relatively large areas of mainly positive differences were also shown to be
689 detected in the higher latitudes, especially in the Atlantic and Pacific basins. Overall,
690 although the normalized U_{10} biases were shown to be mostly below 36%, these
691 differences could be responsible for both local and remote misrepresentation of the wave
692 fields on all ensemble members.

693 The global normalized (Figs. 3 and 4) and absolute (Fig. 5) biases between each
694 ensemble member and ERA5 for the mean H_S , T_m and MWD , and 95% percentile H_S and
695 T_m , versus ERA5, revealed considerably distinct patterns for each model-
696 parameterization pair. Overall, the consistently best-performing ensemble members were
697 shown to be PC20-3 (WW3-ST4) and -4 (WW3-ST6). While most members tended to
698 overestimate H_S and T_m at a global scale, especially in the extratropical latitudes, PC20-
699 1 (WW3-ST2) and -6 (SWAN-ST6) showed a consistent opposite behavior. Within the
700 WW3 simulations (PC20-1 to -4), despite the different STs, uncertainty was shown to
701 remain relatively contained. However, the integration of the remaining simulations led to
702 a considerable decrease in the ensemble's robustness. SWAN runs (PC20-5 and -6), in
703 particular, not only showed systematically different behaviors between each other, but
704 also in comparison to other model-parameterization pairs. Despite sharing a similar
705 configuration, SWAN-ST6 (PC20-6) and WW3-ST6 (PC20-4) revealed a distinct
706 representation of the wave climate in Figs. 3 to 9, 12 and Tables 1 to 4, especially in the
707 extratropical areas. As it was shown in Sections 2.2.1. and 2.2.2., as well as in Table SM1,
708 the implementation of the ST6 parameterization in WW3 and SWAN revealed slight
709 dissimilarities (*e.g.*, U_{10} scaling factors and swell dissipation terms) which may have
710 contributed to the distinct representations of the global wave climate. A similar contrast
711 was shown to be visible for the WW3-ST3 (PC20-2) and WAM4.6 (PC20-7) simulations,
712 which produced slightly different global outputs despite their numerical similarities.

713 Fig. 13 reveals the present climate normalized ensemble inter-member uncertainty
714 range (NUR) considering the full (7-member) ensemble (top), the WW3 subset (middle),

715 and the SWAN subset (bottom), respectively. In the context of climate projections, the
 716 NUR represents the minimum ensemble/subset projected change necessary to exceed the
 717 present climate ensemble spread. Fig. SM13 is similar to Fig. 13, but for T_m . Both figures
 718 show that for the WW3 subset of the ensemble (Fig. 13c,d and SM13c,d), the NUR
 719 reaches up to 20% in the extratropical latitudes, and up to 50% (H_S) and 30% (T_m) in the
 720 tropical areas. On the other hand, the two SWAN simulations induce spreads within 30%–
 721 40% (60%–70%) at the extratropical (tropical) latitudes, for the mean H_S (Fig. 13e), and
 722 up to 30% across most of the global ocean for T_m (Fig. SM13e). Considering the full
 723 ensemble, the NUR attains values above 70% in the tropical Atlantic, Pacific and Indian
 724 basins, for both the mean and 95% percentile H_S (Fig. 13a,b), remaining above 30% in
 725 the remaining global ocean. For T_m , these values range between 30% and 40% for the
 726 mean and extremes in most locations (Fig. SM13a,b). The seasonal NURs, in Figs. SM11
 727 (DJF) and SM12 (JJA) for H_S , and SM14 (DJF) and SM15 (JJA) for T_m , are consistent
 728 with the ones at an annual scale, despite slightly higher values in the respective summer
 729 hemisphere. Note that, overall, the NURs found for both the H_S and T_m surpass even the
 730 highest emission scenario projections obtained for these parameters towards the end of
 731 the 21st century, in recent scientific literature (e.g., Hemer *et al.*, 2013a; Semedo *et al.*,
 732 2013; Wang *et al.*, 2015; Lemos *et al.*, 2020b; albeit for CMIP3 and CMIP5). Ensemble
 733 spreads of such magnitudes can lead to serious robustness issues within future projected
 734 changes in wave climate. It should be highlighted that a single-forcing EC-Earth3
 735 simulation was used here, and therefore, a multi-forcing approach under similar
 736 conditions could potentially lead to even greater NURs.

737 The comparison between the PC20 ensemble members and *in-situ* observations, in
 738 Fig. 6, revealed a reasonable agreement for all model-parameterization pairs across five
 739 different regional areas, for both H_S and T_p . Overall, the main behavior of each member
 740 was shown to be similar to those represented in Figs. 3 and 4 (for T_m , nevertheless). Biases
 741 were shown to generally increase towards the higher quantiles and assume positive values
 742 (Tables 2 and 4). Exceptions include PC20-2 (WW3-ST3) and -3 (WW3-ST4) H_S and
 743 PC20-1 (WW3-ST2) T_p across ETNA, and most members across ETNP (T_p). For H_S (T_p),
 744 the lowest RMSEs and SIs combined with the highest Rs were found for the ETNP
 745 (TWSP/ETSP) area, despite the higher mean biases when compared to ETNA and TNAO
 746 (Tables 1 and 3). Regarding the mean annual cycles, the PC20 ensemble was shown to
 747 be in better agreement with observations for H_S than for T_p , especially across ETNP and
 748 TWSP/ETSP. In these areas, both PC20-5 (SWAN-ST1) and -7 (WAM4.6) struggled to
 749 depict a correct T_p intra-annual climatology. A similar misrepresentation was visible for
 750 PC20-5 across ETNA. It should be noted, however, that in Fig. 9, the mean intra-annual
 751 cycles for T_m show a relatively accurate depiction from all ensemble members, despite
 752 the consistent biases compared to ERA5.

753 The H_S M-scores shown in Fig. 12a revealed a better overall agreement between
 754 ensemble members and ERA5 across the extratropical areas, with average values ranging
 755 between 700 and 900. In the tropical regions, not only was the inter-member M-score
 756 range shown to be greater, revealing less consistency in the overall performance, but the
 757 mean values were also shown to be lower, mostly between 500 and 800, and down to the
 758 200–400 range for TENP and TESP. These areas were also shown to be the most
 759 challenging for T_m , with a mean M-score of approximately 200 for TESP. The highly
 760 variable sea state conditions across the eastern Pacific basin, dominated by both the long
 761 swells from the Southern Ocean (Lemos *et al.*, 2021b) and local tropical phenomena,

762 contribute to lower modelling performance across TENP and TESP, also noted by
763 Semedo *et al.* (2018a).

764 Finally, Fig. 14 shows the normalized biases (in %) from the comparison between
765 the democratically built PC20 ensemble H_S , T_m and MWD annual means and extremes
766 (for H_S and T_m), and ERA5, similar to the initially presented in Figs. 3, 4 and 5 for each
767 ensemble member. For the three wave parameters, it is clear that the performance of the
768 PC20 ensemble as a whole is far better than the ones from each model-parameterization
769 pair. In fact, Figs. 14a,b show that for the annual mean (95% percentile) H_S , differences
770 range from -20% to 12% at a global scale, except in the Maritime Continent (higher
771 latitudes of the Southern Ocean – due to undersampling issues caused by sea ice cover),
772 where slightly greater positive differences can be found. Similar normalized biases can
773 be found for T_m , ranging between -12% and 20%, whereas for the MWD differences are
774 only evident at the tropical and subtropical latitudes of the NH (areas dominated by local
775 tropical phenomena). For the three parameters, normalized and absolute biases attain
776 slightly higher values during the extreme seasons (Figs. SM16 and SM17 in the SM),
777 ranging nevertheless between -28% and 20% for H_S , -12% and 28% for T_m and generally
778 below 36° for MWD .

779 The performance assessment carried out in this study, with specific focus on wave
780 model and physical parameterization uncertainty sources, led to two major conclusions.
781 The first being that all PC20 ensemble members are able to reasonably represent the
782 reference wave climate (both reanalyzed and observed), especially PC20-3 (WW3-ST4)
783 and -4 (WW3-ST6), for which the overall accuracy was shown to be the highest. Finally,
784 as an ensemble, PC20 was shown to perform better than each of its individual members.
785 Secondly, however, despite the increased agreement with observations, changing the
786 wave-model-parameterization combinations within PC20 ensemble members was shown
787 to be enough to produce considerable spreads for the analyzed variables. The impact of
788 this specific uncertainty source in the future wave climate projection ensembles requires
789 further investigation. Nevertheless, it should be highlighted that substantial progress has
790 been recently achieved in improving the global and regional wave climate description by
791 wave models. A dedicated focus on reducing the wave-model-parameterization source of
792 uncertainty in future assessments is paramount for modelling teams, and preference
793 should be given to more recent and balanced parameterizations.

794 **Acknowledgements**

795 This work was funded by the Portuguese Fundação para a Ciência e a Tecnologia (FCT)
796 I.P./MCTES through national funds (PIDDAC) – UIDB/50019/2020.

Journal Pre-proof

797

5. References

798

- 799 Aarnes, O. J., Breivik, Ø., Reistad, M. (2012). Wave extremes in the Northeast Atlantic.
800 *J. Clim.*, 25, 1529–1543. DOI: 10.1175/JCLI-D-11-00132.1.
- 801 Aarnes, O. J., Abdalla, S., Bidlot, J.-R., Breivik, Ø. (2015). Marine Wind and Wave
802 Height Trends at Different ERA-Interim Forecast Ranges. *J. Clim.*, 28, 819–837.
- 803 Almar, R., Ranasinghe, R., Bergsma, E. W. J., Diaz, H., Melet, A., Papa, F., Vousdoukas,
804 M., Athanasiou, P., Dada, O., Almeida, L. P., Kestenare, E. (2021). A global analysis
805 of extreme coastal water levels with implications for potential coastal overtopping.
806 *Nature Communications*, 12, 3775. DOI: [https://doi.org/10.1038/s41467-021-24008-](https://doi.org/10.1038/s41467-021-24008-9)
807 9.
- 808 Alves, J. H. G. M. (2006). Numerical modelling of ocean swell contributions to the global
809 wind-wave climate. *Ocean Modell.*, 11, 98–122.
- 810 Amante, C., Eakins, B. (2009). ETOPO1 1 Arc-minute Global Relief Model: Procedures,
811 Data sources and Analysis. NOAA Technical Memorandum NESDIS (NGDC-24),
812 1-25.
- 813 Ardhuin, F., Rogers, E., Babanin, A. V., Filipot, J.-F., Magne, R., Roland, A., Van der
814 Westhuysen, A., Queffelec, P., Lefevre, J.-M., Aouf, L., Collard, F. (2010).
815 Semiempirical Dissipation source functions for ocean waves. Part I: definition,
816 calibration, and validation, *J. Phys. Oceanogr.*, 40, 1917–1941. DOI:
817 <http://dx.doi.org/10.1175/2010JPO4324.1>.
- 818 Babanin, A. V., Onorato, M., Qiao, F. (2012). Surface waves and wave-coupled effects
819 in lower atmosphere and upper ocean. *J. Geophys. Res.*
820 <https://doi.org/10.1029/2012JC007932>. C00J01.
- 821 Babanin, A.V. (2011). *Breaking and Dissipation of Ocean Surface Waves*. Cambridge
822 University Press, 480, pp.
- 823 Barnard, P. L., Short, A., Harley, M. D., Splinter, K. D., Vitousek, S., Turner, I. L., Allan,
824 J., Banno, M., Bryan, K. R., Doria, A., Hansen, J. E., Kato, S., Kuriyama, Y.,
825 Randall-Goodwin, E., Ruggiero, P., Walter, I. J., Heathfield, D. K. (2015). Coastal
826 vulnerability across the Pacific dominated by El Niño/Southern Oscillation. *Nature*
827 *Geosciences*, 8, 801–807.
- 828 Barnard, P. L., Hoover, D., Hubbard, D. M., Snyder, A., Ludka, B., Allan, J., Kaminsky,
829 M., Ruggiero, P., Gallien, T. W., Gabel, L., McCandless, D., Weiner, H. M., Cohn,
830 N., Anderson, D., Serafin, K. A. (2017). Extreme oceanographic forcing and coastal
831 response due to the 2015–2016 El Niño. *Nature Communications*, 8, 14365. Battjes
832 and Janssen (1978)
- 833 Bidlot, J.-R., Holmes, D. J., Wittmann, P. A., Lalbeharry, R., Chen, H. S. (2002).
834 Intercomparison of the performance of operational ocean wave forecasting systems
835 with buoy data. *Weather Forecasting*, 17, 287–310.
- 836 Bidlot, J.-R., Janssen, P., Abdalla, S. (2005). A revised formulation for ocean wave
837 dissipation in CY29R1. ECMWF Technical Memorandum, R60.9/JB/0(1), 1–35.
- 838 Bidlot J.-R., Janssen, P., Abdalla, S. (2007). A revised formulation of ocean wave
839 dissipation and its model impact. ECMWF Tech. Memo. 509. ECMWF, Reading,
840 United Kingdom, 27pp. Available online at: <http://www.ecmwf.int/publications/>.
- 841 Bidlot J.-R., Li, J.-G., Wittmann, P., Faucher, M., Chen, H., Lefevre, J.-M., Bruns, T.,
842 Greenslade, D., Ardhuin, F., Kohno, N., Park, S., Gomez, M. (2007). Inter-
843 Comparison of Operational Wave Forecasting Systems. Proc. 10th International
844 Workshop on Wave Hindcasting and Forecasting and Coastal Hazard Symposium,

- 845 North Shore, Oahu, Hawaii, November 11-16, 2007.
846 <http://www.waveworkshop.org/10thWaves/ProgramFrameset.htm>.
- 847 Bidlot, J.-R. (2017). Twenty-one years of wave forecast verification. ECMWF newsletter,
848 No 150, 31-36. DOI: 10.18442/ECMWF-NL-201610.
- 849 Bidlot, J.-R., Lemos, G., Semedo, A., The C3S Reanalysis Team, ECMWF. (2019,
850 November). ERA5 reanalysis & ERA5 based ocean wave hindcast. Presented at the
851 2nd International Workshop on Waves, Storm Surges and Coastal Hazards,
852 Melbourne, Australia. Retrieved from
853 [http://waveworkshop.org/16thWaves/Presentations/R1%20Wave_Workshop_2019](http://waveworkshop.org/16thWaves/Presentations/R1%20Wave_Workshop_2019_Bidlot_et_al.pdf)
854 [_Bidlot_et_al.pdf](http://waveworkshop.org/16thWaves/Presentations/R1%20Wave_Workshop_2019_Bidlot_et_al.pdf)
- 855 Bitner-Gregersen, E. M., Eide, L. I., Hørte, T., Vanem, E. (2015). Impact of Climate
856 Change and Extreme Waves on Tanker Design. SNAME Transactions 2014, USA.
- 857 Bitner-Gregersen, E. M., Gramstad, O. (2018). Potential changes in the joint probabilistic
858 description of the North Atlantic wave climate. Proceedings of the ASME 2018 37th
859 International Conference on Ocean, Offshore and Arctic Engineering - OMAE2018,
860 June 17–22, 2018, Madrid, Spain.
- 861 Booij, N., Holthuijsen, L. H., Ris, R. C. (1996). THE “SWAN” WAVE MODEL FOR
862 SHALLOW WATER. Coastal Engineering, 53, 668-676.
- 863 Booij, N., Ris, R. C., Holthuijsen, L. H. (1999). A third-generation wave model for coastal
864 regions: 1. Model description and validation. Journal of Geophysical Research
865 Oceans, 104, C4, 7649-7666. DOI: <https://doi.org/10.1029/98JC02622>.
- 866 Bricheno, L. M., Wolf, J. (2018). Future Wave Conditions of Europe, in Response to
867 High-End Climate Change Scenarios. Journal of Geophysical Research: Oceans, 123,
868 8762–8791. DOI: <https://doi.org/10.1029/2018JC013866>.
- 869 Caires, S., Swail, V. R. (2004). Global wave climate trend and variability analysis.
870 Proceedings of the. Eighth International Workshop on Wave Hindcasting and
871 Forecasting, Oahu, HI, U.S. Army Engineer Research and Development Center’s
872 Coastal and Hydraulics Laboratory and Cosponsors, Al.
873 [<http://www.waveworkshop.org/8thWaves/Papers/A1.pdf>.]
- 874 Camus, P., Losada, I. J., Izaguirre, C., Espejo, A., Menéndez, M., Pérez, J. (2017).
875 Statistical wave climate projections for coastal impact assessments. Earth's Future 5,
876 918-933, doi:doi:10.1002/2017EF000609.
- 877 Casas-Prat, M., Wang, X. L., Swart, N. (2018). CMIP5-based global wave climate
878 projections including the entire Arctic Ocean. Ocean Model, 123, 66–85.
- 879 Cavaleri, L., Fox-Kemper, B., Hemer, M. A. (2012). Wind waves in the coupled climate
880 system. Bulletin of the American Meteorological Society, 93, 1651-1661.
- 881 Cazenave, A., Cozannet, G. L. (2014). Sea level rise and its coastal impacts. Earth’s
882 Future, 2, 15-34.
- 883 De Leo, F., Besio, G., Zolezzi, G., Bezzi, M. (2019). Coastal vulnerability assessment:
884 through regional to local downscaling of wave characteristics along the Bay of Lalzit
885 (Albania). Natural Hazards Earth Syst. Sci., 19, 287-298. DOI:
886 <https://doi.org/10.5194/nhess-19-287-2019>.
- 887 Dietrich, J., Zijlema, M., Westerink, J., Holthuijsen, L., Dawson, C., Luettich Jr., R.,
888 Jensen, R., Smith, J., Stelling, G., Stone, G. (2011). Modeling hurricane waves and
889 storm surge using integrally-coupled, scalable computations, Coast. Eng., 58, 45–65.
- 890 Dobrynin, M., Murawsky, J., Yang, S. (2012). Evolution of the global wind wave climate
891 in CMIP5 experiments. Geophysical Research Letters, 39,
892 DOI:10.1029/2012GL052843.
- 893 Dobrynin, M., Murawski, J., Baehr, J., Ilyina, T. (2015). Detection and Attribution of
894 Climate Change Signal in Ocean Wind Waves. Journal of Climate, 28, 4, 1578-1591.

- 895 Döscher, R., Acosta, M., Alessandri, A., Anthoni, P., Arneth, A., Arsouze, T., Bergmann,
896 T., Bernadello, R., Bousetta, S., Caron, L.-P., Carver, G., Castrillo, M., Catalano, F.,
897 Cvijanovic, I., Davini, P., Dekker, E., Doblas-Reyes, F. J., Docquier, D., Echevarria,
898 P., Fladrich, U., Fuentes-Franco, R., Gröger, M., v. Hardenberg, J., Hieronymus, J.,
899 Karami, M. P., Keskinen, J.-P., Koenigk, T., Makkonen, R., Massonnet, F.,
900 Ménégos, M., Miller, P. A., Moreno-Chamarro, E., Nieradzic, L., van Noije, T.,
901 Nolan, P., O'Donnell, D., Ollinaho, P., van den Oord, G., Ortega, P., Prims, O. T.,
902 Ramos, A., Reerink, T., Rousset, C., Ruprich-Robert, Y., Le Sager, P., Schmith, T.,
903 Schrödner, R., Serva, F., Sicardi, V., Sloth Madsen, M., Smith, B., Tian, T.,
904 Tourigny, E., Uotila, P., Vancoppenolle, M., Wang, S., Wårlind, D., Willén, U.,
905 Wyser, K., Yang, S., Yepes-Arbós, X., Zhang, Q. (2022). The EC-Earth3 Earth
906 System Model for the Climate Model Intercomparison Project 6. *Geosci. Model*
907 *Dev.*, 15, 2973–3020. DOI: <https://doi.org/10.5194/gmd-15-2973-2022>.
- 908 ECMWF. (2016). IFS Documentation CY41R2. <https://www.ecmwf.int/node/16651>.
- 909 ECMWF. (2018). IFS Documentation CY45R1 - Part VII : ECMWF Wave Model.
910 <https://www.ecmwf.int/node/18717>.
- 911 Erikson, L. H., Hegermiller, C. A., Barnard, P. L., Ruggiero, P., van Ormondt, M. (2015).
912 Projected wave conditions in Eastern North Pacific under the influence of two
913 CMIP5 climate scenarios. *Ocean Modelling*, 96, 1, 171-185.
- 914 Falloon, P., Challinor, A., Dessai, S., Hoang, L., Johnson, J., Koehler, A.-K. (2014).
915 Ensembles and uncertainty in climate change impacts. *Frontiers in Environmental*
916 *Science*, 2, 33. doi: 10.3389/fenvs.2014.00033.
- 917 Fan, Y., Held, I. M., Lin, S.-J., Wang, X. L. (2013). Ocean warming effect on surface
918 gravity wave climate change for the end of the 21st century. *Journal of Climate*, 26,
919 6046-6066.
- 920 Foley, A. (2010). Uncertainty in Regional Climate Modelling: A Review. *Progress in*
921 *Physical Geography*, 34(4). doi:10.1177/0309133310375654.
- 922 Harley, M. D., Turner, I. L., Kinsela, M. A., Middleton, J. H., Mumford, P. J., Splinter,
923 K. D., Phillips, M. S., Simmons, J. A., Hanslow, D. J., Short, A. (2017). Extreme
924 coastal erosion enhanced by anomalous extratropical storm wave direction. *Scientific*
925 *Reports*, 7, 6033.
- 926 Hasselmann, K., Barnett, T. P., Bouws, E., Carlson, H., Cartwright, D. E., Enke, K.,
927 Ewing, J. A., Gienapp, H., Hasselmann, D. E., Kruseman, P., Meerburg, A., Müller,
928 P., Olbers, D. J., Richter, K., Sell, W., Walden, H. (1973). Measurements of wind-
929 wave growth and swell decay during the Joint North Sea Wave Project (JONSWAP),
930 *Deutsche Hydrographische Zeitschrift.*, Suppl. A, 8(12), 95p.
- 931 Hasselmann, S., Hasselmann, K., Allender, J.H., Barnett, T.P. (1985). Computations and
932 parameterizations of the nonlinear energy transfer in a gravity-wave spectrum. Part
933 II: Parameterizations of the nonlinear energytransfer for application in wave models.
934 *J. Phys. Oceanogr.* 15, 1378–1391.
- 935 Hawkins, E., Sutton, R. (2009). The potential to narrow uncertainty in regional climate
936 predictions. *Bulletin of the American Meteorological Society*, 90, 1095–1107.
- 937 Hemer, M. A., Katzfey, J., Trenham, C. E. (2013a). Global dynamical projections of
938 surface ocean wave climate for a future high greenhouse gas emission scenario.
939 *Ocean Modelling*, 70, 221-245.
- 940 Hemer, M. A., Trenham, C. E. (2016). Evaluation of a CMIP5 derived dynamical global
941 wind wave climate model ensemble. *Ocean Modelling*, 103, DOI:
942 10.1016/j.ocemod.2015.10.009.IPCC-AR5. *Climate Change 2014: The Physical*
943 *Science Basis*; Cambridge University Press: Cambridge, UK, 2014.

- 944 Hersbach, H., Bell, B., Berrisford, P., Hirahara, S., Horányi, A., Muñoz-Sabater, J.,
945 Nicolas, J., Peubey, C., Radu, R., Schepers, D., Simmons, A., Soci, C., Abdalla, S.,
946 Abellan, X., Balsamo, G., Bechtold, P., Biavati, G., Bidlot, J., Bonavita, M., Chiara,
947 G., Dahlgren, P., Dee, D., Diamantakis, M., Dragani, R., Flemming, J., Forbes, R.,
948 Fuentes, M., Geer, A., Haimberger, L., Healy, S., Hogan, R., Hólm, E., Janisková,
949 M., Keeley, S., Laloyaux, P., Lopez, P., Lupu, C., Radnoti, G., de Rosnay, P., Rozum,
950 I., Vamborg, F., Villaume, S., Thépaut, J. (2020). The ERA5 global reanalysis.
951 *Quarterly Journal of the Royal Meteorological Society*, 2020, 1-51.
- 952 Högström, U., Smedman, A., Sahleé, E., Drennan, W. M., Kahma, K. K., Pettersson, H.,
953 Zhang, F. (2009). The atmospheric boundary layer during swell: A field study and
954 interpretation of the turbulent kinetic energy budget for high wave ages. *Journal of*
955 *Atmospheric Science*, 66, 2764-2779.
- 956 Högström, U., Smedman, A.-S., Semedo, A., Rutgersson, A. (2011). Comments on “A
957 global climatology of wind wave interaction”. *Journal of Physical Oceanography*, 41,
958 1811–1813.
- 959 Janssen, P. A. E. M. (2004). *The Interaction of Ocean Waves and Wind*. Cambridge:
960 Cambridge University Press.
- 961 Jeffreys, H. (1924). On the formation of waves by wind. *Proceedings of the Royal*
962 *Society*, A107, 189-206.
- 963 Jeffreys, H. (1925). On the formation of waves by wind II. *Proceedings of the Royal*
964 *Society*, A110, 341–347.
- 965 Jones, R. N. et al. in *Climate Change 2014: Impacts, Adaptation, and Vulnerability* (eds
966 Field, C. B. et al.) Ch. 2 (IPCC, Cambridge Univ. Press, 2014).
- 967 Kamranzad, B., Etemad-Shahidi, A., Chegini, V., Yeganeh-Bakhtiary, A. (2015). Climate
968 change impact on wave energy in the Persian Gulf. *Climate Dynamics*, 65, 777-794.
969 DOI: <https://doi.org/10.1007/s10236-015-0833-y>.
- 970 Kamranzad, B., Mori, N. (2018). Regional Wave Climate Projection Based on Super-
971 High-Resolution MRI-AGCM3.2S, Indian Ocean. *Journal of Japan Society of Civil*
972 *Engineers*, 74, 2, 1351-1355. DOI: https://doi.org/10.2208/kaigan.74.I_1351.
- 973 Kamranzad, B., Mori, N. (2019). Future wind and wave climate projections in the Indian
974 Ocean based on a super-high-resolution MRI-AGCM3.2S model projection. *Climate*
975 *Dynamics*, 53, 2391-2410. DOI: <https://doi.org/10.1007/s00382-019-04861-7>.
- 976 Kirezci, E., Young, I. R., Ranasinghe, R., Muis, S., Nicholls, R. J., Lincke, D., Hinkel, J.
977 (2020). Projections of global-scale extreme sea levels and resulting episodic coastal
978 flooding over the 21st Century. *Scientific Reports*, 10, 11629. DOI:
979 <https://doi.org/10.1038/s41598-020-67736-6>.
- 980 Knutti, R., Sedláček, J. (2012). Robustness and uncertainties in the new CMIP5 climate
981 model projections. *Nature Climate Change*, 3, 369–373.
- 982 Komen, G. J., Cavalieri, L., Doneland, M., Hasselmann, S., Janssen, P. A. E. M. (1994).
983 *Dynamics and modeling of ocean waves*. Cambridge: Cambridge University Press.
- 984 Kumar, R., Lemos, G., Semedo, A., Alsaaq, F. (2022). Parameterization-Driven
985 Uncertainties in Single-Forcing, Single-Model Wave Climate Projections from a
986 CMIP6-Derived Dynamic Ensemble. *Climate*, 10, 51. DOI:
987 <https://doi.org/10.3390/cli10040051>.
- 988 Lemos, G., Semedo, A., Dobrynin, M., Behrens, A., Staneva, J., Bidlot, J.-R., Miranda,
989 P. (2019). Mid-twenty-first century global wave climate projections: Results from a
990 dynamic CMIP5 based ensemble. *Global and Planetary Change*, 172, 69-87.
- 991 Lemos, G., Menendez, M., Semedo, A., Camus, P., Hemer, M., Dobrynin, M., Miranda,
992 P. (2020a). On the need of bias correction methods for wave climate projections.
993 *Global and Planetary Change*, 186, 103109.

- 994 Lemos, G., Semedo, A., Dobrynin, M., Menendez, M., Miranda, P. (2020b). Bias-
995 Corrected CMIP5-Derived Single-Forcing Future Wind-Wave Climate Projections
996 toward the End of the Twenty-First Century. *Journal of Applied Meteorology and*
997 *Climatology*, 59, 9, 1393–1414. <http://dx.doi.org/10.1175/jamc-d-19-0297.1>
- 998 Lemos, G., Semedo, A., Menendez, M., Miranda, P. M. A., Hemer, M. (2021a). On the
999 decreases in North Atlantic significant wave heights from climate projections.
1000 *Climate Dynamics*. DOI: <https://doi.org/10.1007/s00382-021-05807-8>.
- 1001 Lemos, G., Semedo, A., Hemer, M., Menendez, M., Miranda, P. M. A.. (2021b). Remote
1002 climate change propagation across the oceans – the directional swell signature.
1003 *Environmental Research Letters*. DOI: <https://doi.org/10.1088/1748-9326/ac046b>.
- 1004 Liang, B., Gao, H., Shao, Z. (2019). Characteristics of global waves based on the third-
1005 generation wave model SWAN. *Marine Structures*, 64, 35-53.
- 1006 Lionello, P., Malguzzi, P., Buzzi, A. (1998). Coupling between the Atmospheric
1007 Circulation and the Ocean Wave Field: An Idealized Case. *Journal of Physical*
1008 *Oceanography*, 21, 161-177.
- 1009 Lobeto, H., Menendez, M., Losada, I. (2021a). Future behavior of wind wave extremes
1010 due to climate change. *Scientific Reports*, 11, 7869. DOI: 10.1038/s41598-021-
1011 86524-4.
- 1012 Lobeto, H., Menendez, M., Losada, I. (2021b). Projections of Directional Spectra Help to
1013 Unravel the Future Behavior of Wind Waves. *Frontiers in Marine Science*, 8, 558.
1014 DOI: DOI: 10.3389/fmars.2021.655490.
- 1015 Lobeto, H., Menendez, M., Losada, I., Hemer, M. (2022). The effect of climate change
1016 on wind-wave directional spectra. *Global and Planetary Change*, 213(4), 103820.
- 1017 Magnan, A. K., Schipper, E. L. F., Burkett., M., Bharwani, S., Burton, I., Eriksen, S.,
1018 Gemenne, F., Schaar, J., Ziervogel, G. (2016). Addressing the risk of maladaptation
1019 to climate change. *WIREs Climate Change*, 7, 646–665.
- 1020 Melet, A., Meyssignac, B., Almar, R., Le Cozannet, G. (2018). Under-estimated wave
1021 contribution to coastal sea-level rise. *Nature Climate Change*, 8, 234–239.
- 1022 Menendez, M., Mendez, F., Losada, I., Graham, N. (2008). Variability of extreme wave
1023 heights in the northeast Pacific Ocean based on buoy measurements. *Geophysical*
1024 *Research Letters*, 35. DOI: 10.1029/2008GL035394.
- 1025 Meucci, A., Young, I. R., Hemer, M., Trenham, C., Watterson, I. G. (2023). 140 years of
1026 global ocean wind-wave climate derived from CMIP6 ACCESS-CM2 and EC-
1027 Earth3 GCMs: Global trends, regional changes, and future projections. *Journal of*
1028 *Climate*, 36(6), 1605-1631.
- 1029 Mori, N., Yasuda, T., Mase, H., Tom, T., Oku, Y. (2010). Projections of extreme wave
1030 climate change under global warming. *Hydrological Research Letters*, 4, 15-19.
- 1031 Morim, J., Hemer, M. A., Cartwright, N., Strauss, D., Andutta, F. (2018). On the
1032 concordance of 21st century wind-wave climate projections. *Global and Planetary*
1033 *Change*, 167, 160-171.
- 1034 Morim, J., Hemer, M. A., Wang, X., Cartwright, N., Trenham, C., Semedo, A., Young,
1035 I., Bricheno, L., Camus, P., Casas-Prat, M., Erikson, L., Mentaschi, L., Mori, N.,
1036 Shimura, T., Timmermans, B., Aarnes, O., Breivik, Ø., Behrens, A., Dobrynin, M.,
1037 Menendez, M., Staneva, J., Wehner, M., Wolf, J., Kamranzad, B., Webb, A., Stopa,
1038 J., Andutta, F. (2019). Robustness and uncertainties in global multivariate wind-wave
1039 climate projections. *Nature Climate Change*.
- 1040 Morim, J., Wahl, T., Vitousek, S., Santamaria-Aguilar, S., Young, I., Hemer, M. (2023).
1041 Understanding uncertainties in contemporary and future extreme wave events for
1042 broad-scale impact and adaptation planning. *Science Advances*, 9(2). DOI:
1043 10.1126/sciadv.ade3170.

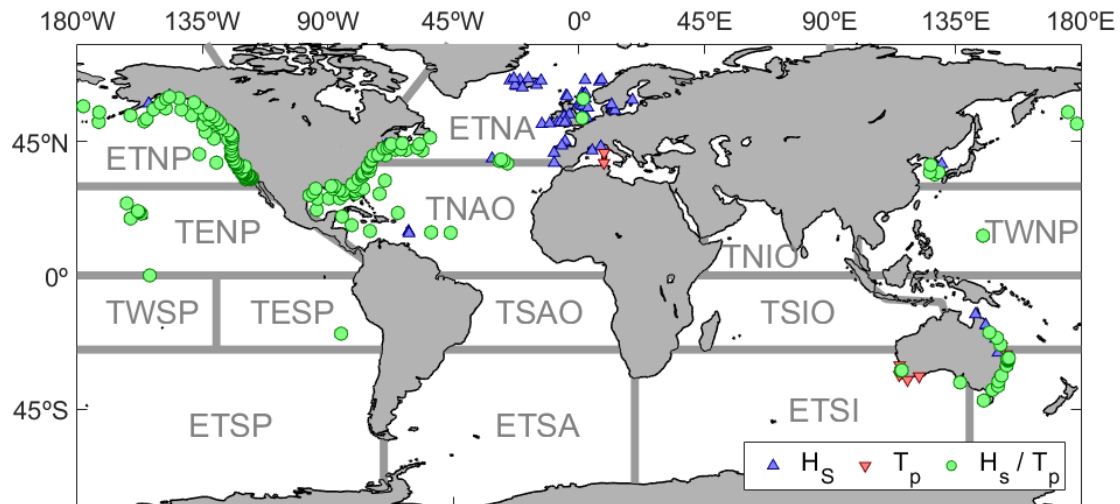
- 1044 NGDC. (2006). 2-minute Gridded Global Relief Data (ETOPO2) v2. NOAA National
1045 Centers for Environmental Information. DOI: <https://doi.org/10.7289/V5J1012Q>.
- 1046 O'Neill, B. C. O., Tebaldi, V., van Vuuren, D. P., Eyring, V., Friedlingstein, P., Hurtt,
1047 G., Knutti, R., Kriegler, E., Lamarque, J.-F., Lowe, J., Meehl, G. A., Moss, R., Riahi,
1048 K., Sanderson, B. M. (2016). The Scenario Model Intercomparison Project
1049 (ScenarioMIP) for CMIP6. *Geosci. Model Dev.*, 9, 3461-3482.
- 1050 Payne, M. R., Barange, M., Cheung, W., MacKenzie, B., Batchelder, H., Cormon, X.,
1051 Eddy, T., Fernandes, J., Hollowed, A., Jones, M., Link, J., Neubauer, P., Ortiz, I.,
1052 Queirós, A., Paula, J. (2015). Uncertainties in projecting climate-change impacts in
1053 marine ecosystems. *ICES Journal of Marine Science*, 73(5), 1272–1282,
1054 <https://doi.org/10.1093/icesjms/fsv231>.
- 1055 Ramon, J., Lledó, L., Torralba, V., Soret, A., Doblas-Reyes, F. J. (2019). What global
1056 reanalysis best represents near-surface winds? *Quarterly Journal of the Royal*
1057 *Meteorological Society*, 145, 3236-3251.
- 1058 Rauser, F., Schemann, V., Sonntag, S. (2015). Sustainable early-career networks. *Nat.*
1059 *Geosci.*, 8, 745–746.
- 1060 Riahi, K., Rao, S., Krey, V., Cho, C., Chirkov, V., Fischer, G., Kindermann, G.,
1061 Nakicenovic, N., Rafaj, P. (2011). RCP 8.5 – a scenario of comparatively high
1062 greenhouse gas emissions. *Climatic Change*, 109, 33-57, DOI: 10.1007/s10584-011-
1063 0149-y.
- 1064 Rogers, W. E., Hwang, P. A., Wang, D. W. (2003). Investigation of wave growth and
1065 decaying the SWAN model: three regional-scale applications. *J. Phys. Oceanogr.*,
1066 33, 366–389.
- 1067 Rogers, W. E., Babanin, A. V., Wang, D. W. (2012). Observation-Consistent Input and
1068 White capping Dissipation in a Model for Wind-Generated Surface Waves:
1069 Description and Simple Calculations. *Journal of Atmospheric and Oceanic*
1070 *Technology*, 29 (9), 1329–1346, doi: 10.1175/JTECH-D-11-00092.1.
- 1071 Ruggiero, P., Komar, P. D., McDougal, W. G., Marra, J. J., Beach, R. A. (2001). Wave
1072 runup, extreme water levels and the erosion of properties backing beaches. *J. Coast.*
1073 *Res.* 2001, 17, 407–419.
- 1074 Rutgersson, A., Sætra, Ø., Semedo, A., Carlson, B., Kumar, R. (2010). Impact of surface
1075 waves in a Regional Climate Model. *Meteorol. Z.*, 19, 3, 247–257.
- 1076 Semedo, A., Sušelj, K., Rutgersson, A. (2008). Variability of Wind Sea and Swell Waves
1077 in the North Atlantic Based on ERA-40 Reanalysis. *Proceedings of the 8th European*
1078 *Wave and Tidal Energy Conference*, September 7-10, 2008, Uppsala, Sweden.
- 1079 Semedo, A., Sætra, Ø., Rutgersson, A., Kahma, K. K., Pettersson, H. (2009). Wave
1080 induced wind in the marine boundary layer. *Journal of Atmospheric Science*, 66,
1081 2256-2271.
- 1082 Semedo, A. (2010). Atmosphere-ocean Interactions in Swell Dominated Wave Fields.
1083 Ph.D. thesis. Uppsala University, Sweden.
- 1084 Semedo, A., Sušelj, K., Rutgersson, A., Sterl, A. (2011). A Global View on the Wind Sea
1085 and Swell Climate and Variability from ERA-40. *Journal of Climate*, 24, 5, 1461-
1086 1479.
- 1087 Semedo, A., Behrens, R., Sterl, A., Bengtsson, L., Günther, H. (2013). Projection of
1088 Global Wave Climate Change toward the End of the Twenty-First Century. *Journal*
1089 *of Climate*, 26, 8269-8288.
- 1090 Semedo, A., Vettor, R., Breivik, Ø., Sterl, A., Reistad, M., Soares, C. G., Lima, D. (2014).
1091 The wind sea and swell waves climate in the Nordic seas. *Ocean Dynamics*, DOI:
1092 10.1007/s10236-014-0788-4.

- 1093 Semedo, A., Dobrynin, M., Lemos, G., Behrens, A., Staneva, J., de Vries, H., Sterl, A.,
1094 Bidlot, J., Döscher, R., Murawski, J., Miranda, P. (2018b). CMIP5 Derived Single-
1095 Forcing, Single-Model and Single-Scenario Wind Wave Climate Simulations:
1096 Ensemble Configuration and Performance Evaluation. *Journal of Marine Science and*
1097 *Engineering*, 6, 90, 28pp.
- 1098 Shih, S. M., Komar, P. D., Tillotson, K. J., McDougal, W.G., Ruggiero, P. (1995). Wave
1099 run-up and sea-cliff erosion. *Coast. Eng.*, 2170–2184.
- 1100 Stocker, T. F., et al., Eds., IPCC. (2013). *Climate Change 2013: The Physical Science*
1101 *Basis. Contribution of Working Group I to the Fifth Assessment Report 1 of the*
1102 *Intergovernmental Panel on Climate Change. Cambridge University Press,*
1103 *Cambridge and New York, 1535 pp.*
- 1104 Stopa, J. E., Cheung, K. F. (2014). Intercomparison of wind and wave data from the
1105 ECMWF reanalysis Interim and the NCEP Climate Forecast System reanalysis.
1106 *Ocean Modelling*, 75, 65-83.
- 1107 Stopa, J. E. (2018). Wind forcing calibration and wave hindcast comparison using
1108 multiple reanalysis and merged satellite wind datasets. *Oceanogr. Meteorol.*, 127,
1109 55–69.
- 1110 Stopa, J. E., Semedo, A., Dobrynin, M., Behrens, A., Staneva, J., Lemos, G. (2019). A
1111 sampling technique to compare climate simulations with sparse satellite
1112 observations: Performance evaluation of a CMIP5 EC-Earth forced dynamical wave
1113 climate ensemble with altimeter observations. *Ocean Modelling*, 134, 18-29.
- 1114 Sullivan, P. P., Edson, J. B., Hristov, T., McWilliams, J. C. (2008). Large-eddy
1115 Simulations and observations of atmospheric marine boundary layers above
1116 nonequilibrium surface waves. *Journal of Atmospheric Science*, 65, 1225-1245.
- 1117 SWAN Team. (2022). *SWAN user manual. SWAN Cycle III version 41.41. Delft*
1118 *University of Technology; 2022. p. 154. Technical documentation.*
- 1119 Tolman, H., Chalikov, D. (1996). Source Terms in a Third-Generation Wind Wave
1120 Model. *Journal of Physical Oceanography*, 26(11), 2497-2518.
- 1121 Chawla, A., Tolman, H. L. (2007). Automated grid generation for WAVEWATCH III.
1122 Tech. Note 254, NOAA/NWS/NCEP/MMAB, 71 pp.
- 1123 Chawla, A., Tolman, H. L. (2008). Obstruction grids for spectral wave models. *Ocean*
1124 *Mod.*, 22, 12–25.
- 1125 Tolman, H. (2009). User manual and system documentation of WAVEWATCH III
1126 version 3.14. NOAA / NWS / NCEP / MMAB Technical Note, 276, 2009.
- 1127 Torralba, V., Doblás-Reyes, F. J. González-Reviriego, N. (2017). Uncertainty in recent
1128 near-surface wind speed trends: a global reanalysis intercomparison. *Environmental*
1129 *Research Letters* 12, 114019, doi:10.1088/1748-9326/aa8a58.
- 1130 Tuomi, L., Kahma, K., Pettersson, H. (2011). Wave hindcast statistics in the seasonally
1131 ice-covered Baltic Sea. *Boreal Environment Research*, 16, 451-472.
- 1132 Vitousek, S., Barnard, P. L., Fletcher, C. H., Frazer, N., Erikson, L., Storlazzi, C. D.
1133 (2017). Doubling of coastal flooding frequency within decades due to sea-level rise.
1134 *Sci. Rep.*, 7, 1399.
- 1135 Vousedoukas, M. I., Mentaschi, L., Voukouvalas, E., Verlaan, M., Jevrejeva, S., Jackson,
1136 L. P., Feyen, L. (2018). Global probabilistic projections of extreme sea levels show
1137 intensification of coastal flood hazard. *Nat. Commun.*, 9, 2360.
- 1138 Wallace, J. M., Deser, C., Smoliak, B. V., Phillips, A. S. (2015). Attribution of Climate
1139 Change in the Presence of Internal Variability. In *Climate Change: Multidecadal and*
1140 *Beyond* (Eds: Chang, C.-P., Ghil, M., Latif, M., Wallace, J. M.), World Scientific.
- 1141 WAMDI Group. (1988). The WAM Model – A Third Generation Ocean Wave Prediction
1142 Model. *Journal of Physical Oceanography*, 18, 1775-1810.

- 1143 Wang, X. L., Feng, Y., Swail, V. R. (2015). Climate change signal and uncertainty in
1144 CMIP5-based projections of global ocean surface wave heights. *Journal of*
1145 *Geophysical Research*, 120, 5, 3859-3871.
- 1146 Watterson, I. G. (1996). Non-dimensional measures of climate model performance. *Int.*
1147 *J. Climatol.*, 16, 379-391.
- 1148 Watterson, I. G., Bathols, J., Heady, C. (2014). What influences the skill of climate
1149 models over the continents? *Bull. Am. Meteorol. Soc.*, 95, 689-700.
- 1150 The WAVEWATCH III Development Group [WW3DG]. (2019). User Manual and
1151 System Documentation of WAVEWATCH III-Version 6.07; Tech. Note 333;
1152 NOAA/NWS/NCEP/MMAB: College Park, MD, USA, 465p.
- 1153 Young, I. R. (1999). Seasonal variability of the global ocean wind and wave climate.
1154 *International Journal of Climatology*, 19, 931-950.
- 1155 Young, I. R., Zieger, S., Babanin, V. (2011). Global trends in wind speed and wave
1156 height. *Science*, 332, 451-455.
- 1157 Zieger, S., Babanin, A. V., Rogers, E. W., Young, I. R. (2015). Observation-based source
1158 terms in the third-generation wave model WAVEWATCH. *Ocean Modelling*, 96, 2–
1159 25.
- 1160 Zijlema, M. van Vledde, G. P., Holthuijsen, L. H. (2012). Bottom friction and wind drag
1161 for wave models. *Coast Eng*, 65, 19–26.
- 1162

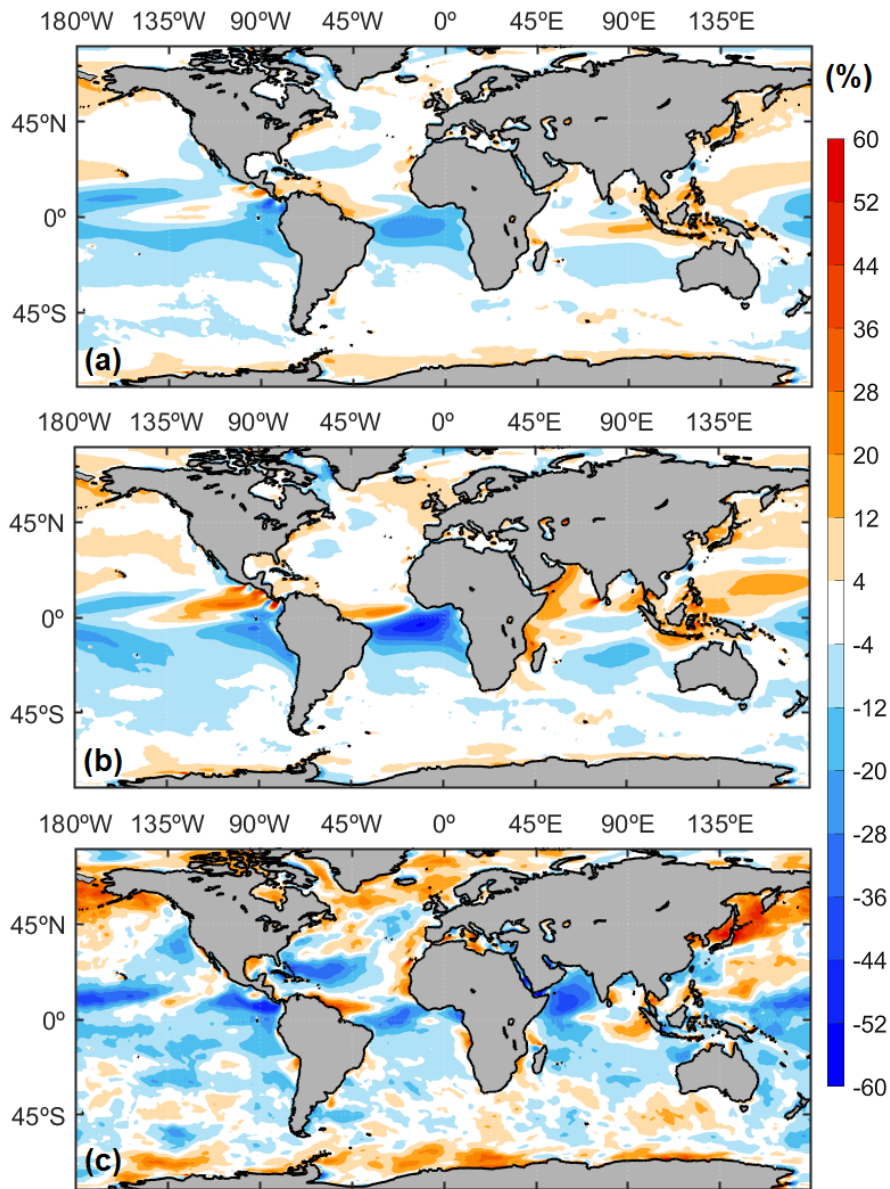
FIGURES AND TABLES

1163
1164
1165
1166



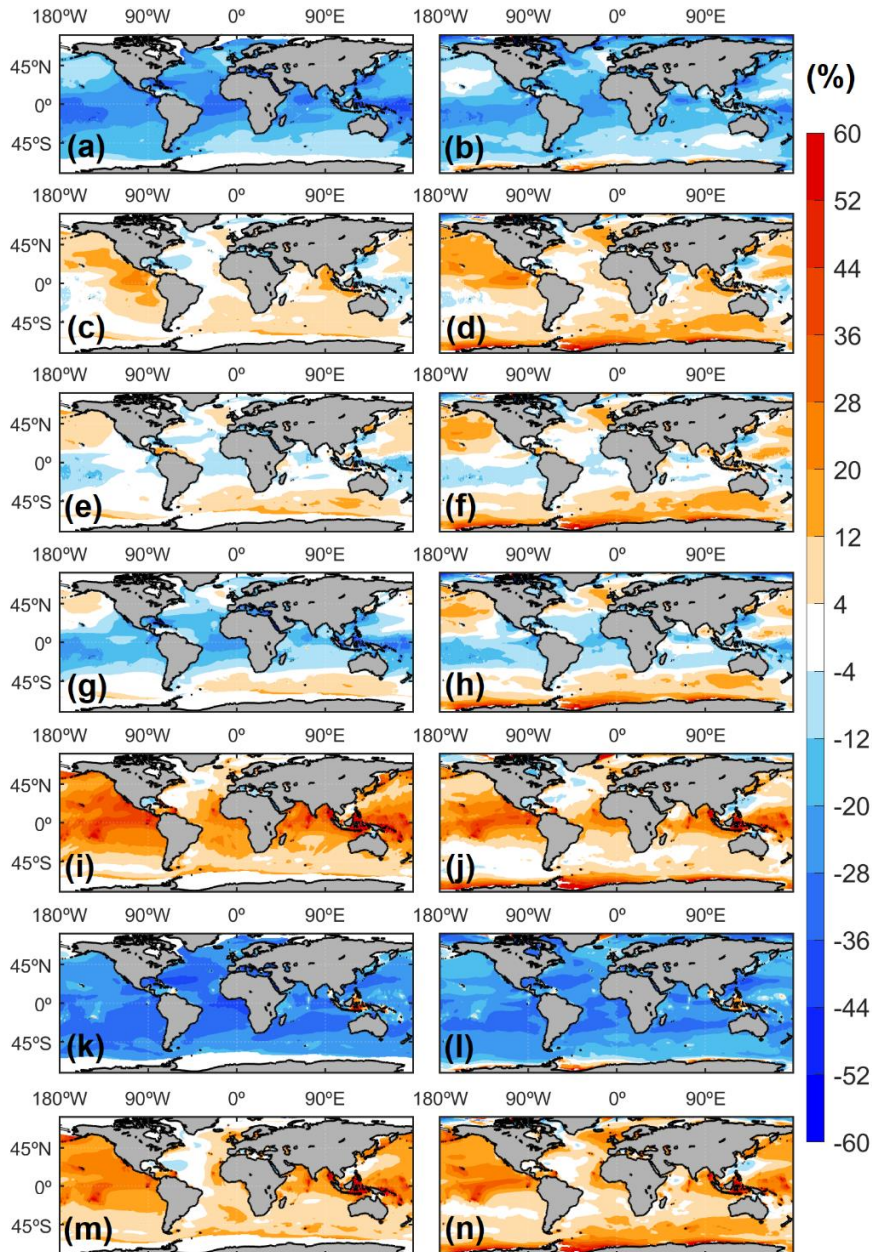
1167
1168
1169
1170
1171
1172
1173
1174
1175
1176

Figure 1 – Map with areas, following Alves (2006). Selected areas: extratropical North Atlantic (ETNA), extratropical South Atlantic (ETSA), extratropical North Pacific (ETNP), extratropical South Pacific (ETSP), extratropical South Indian (ETSI), tropical North Atlantic (TNAO), tropical South Atlantic (TSAO), tropical western North Pacific (TWNP), tropical eastern North Pacific (TENP), tropical western South Pacific (TWSP), tropical eastern South Pacific (TESP), tropical North Indian (TNIO), tropical South Indian (TSIO). Further details can be seen on Table SM1. Selected *in-situ* locations are marked according to the available wave parameters: (blue) H_s , (red) T_p and (green) both.



1177
1178
1179
1180

Figure 2 – Normalized differences (in %) between the (a) annual, (b) DJF and (c) JJA EC-Earth3 and ERA5 U_{10} means for the 1995-2014 historical period.



1181
 1182
 1183
 1184
 1185

Figure 3 – Normalized differences (in %) between the (top) PC20-1 (WW3-ST2) to (bottom) -7 (WAM4.6) ensemble members' and ERA5 (left) annual mean H_5 and (right) 95% percentile H_5 (1995-2014).

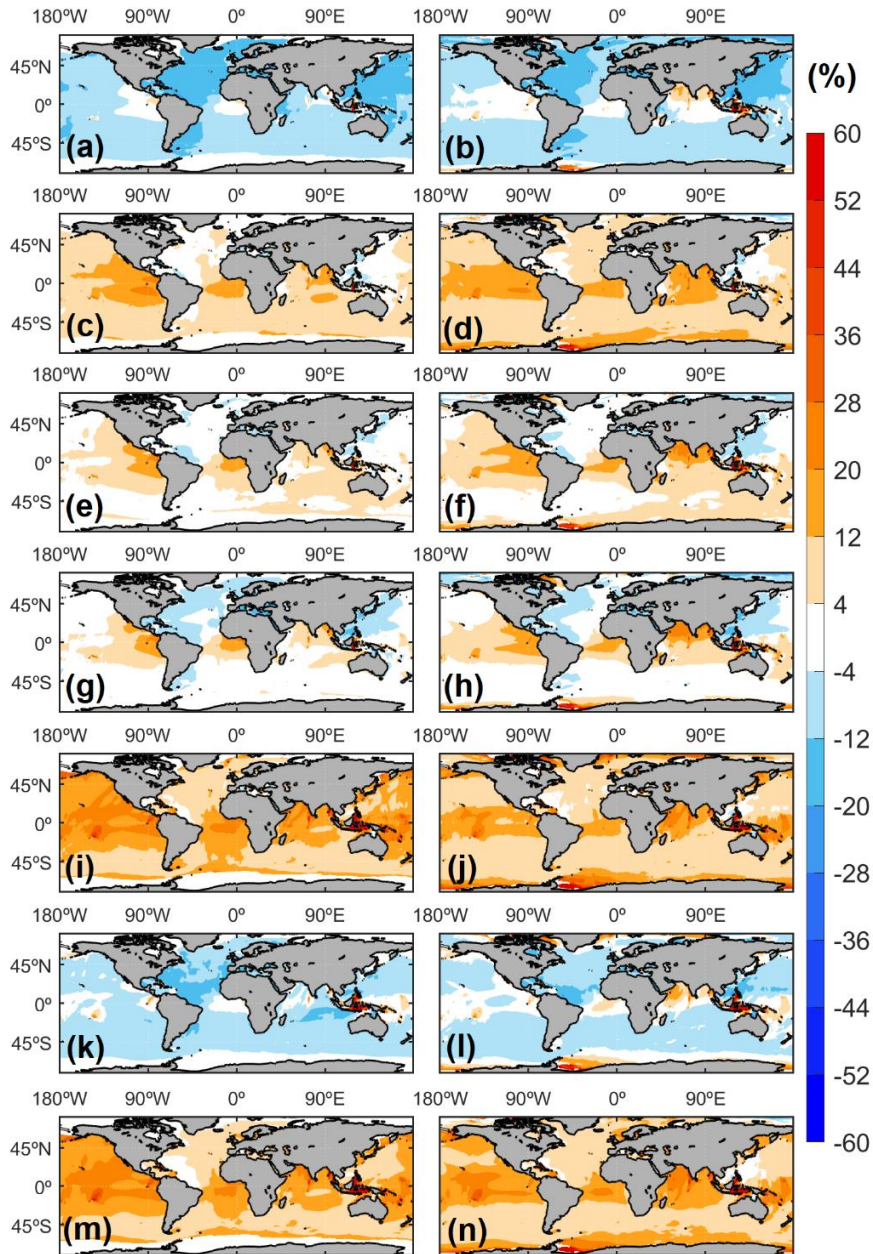
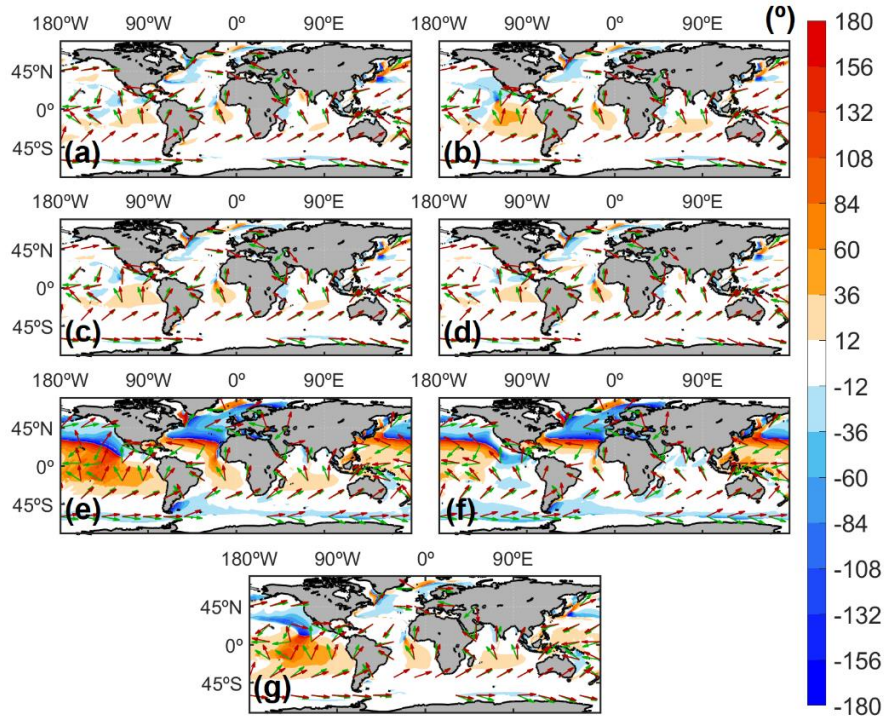


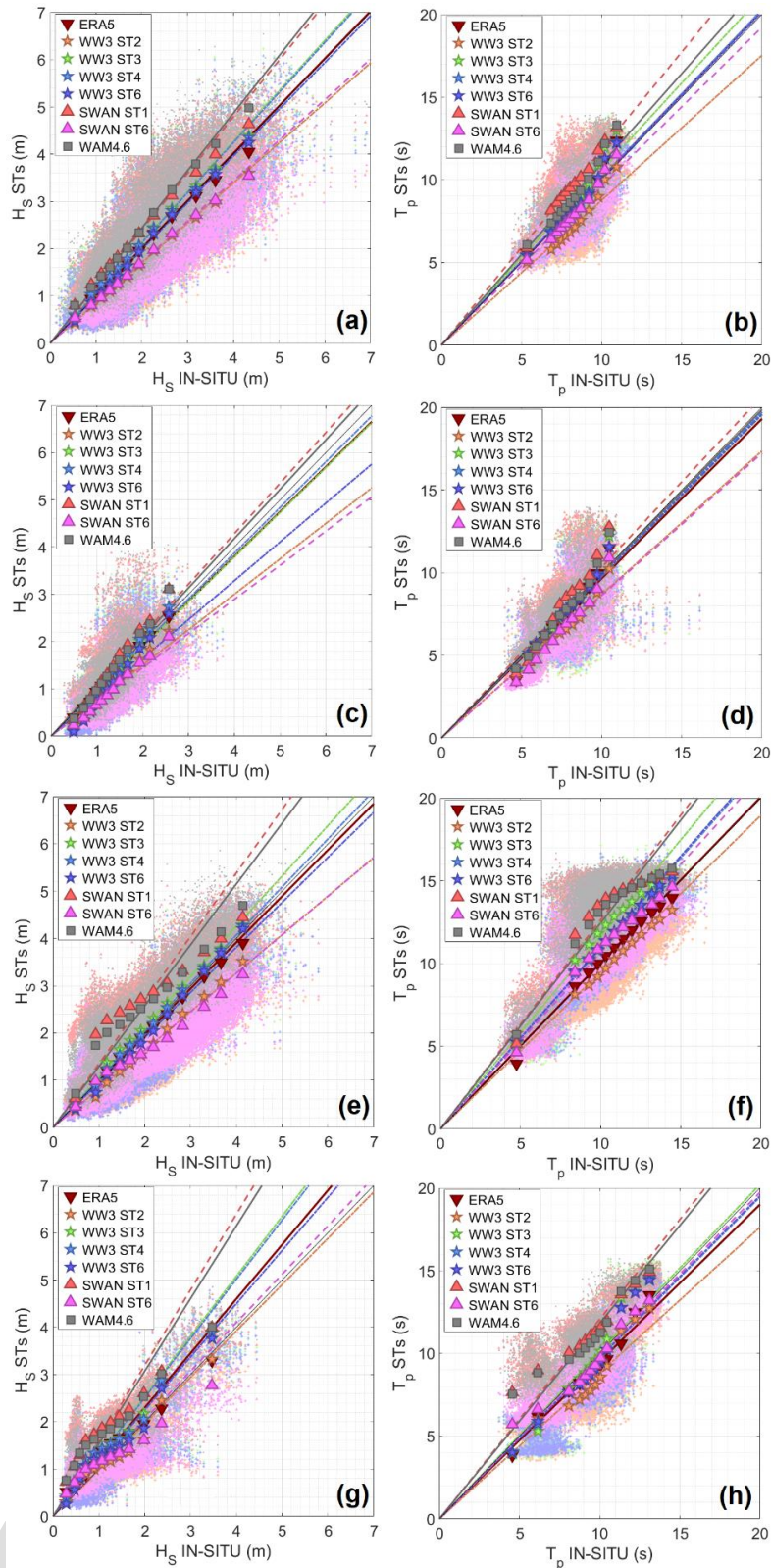
Figure 4 – Same as in Figure 3, but for T_m (s).

1186
1187
1188



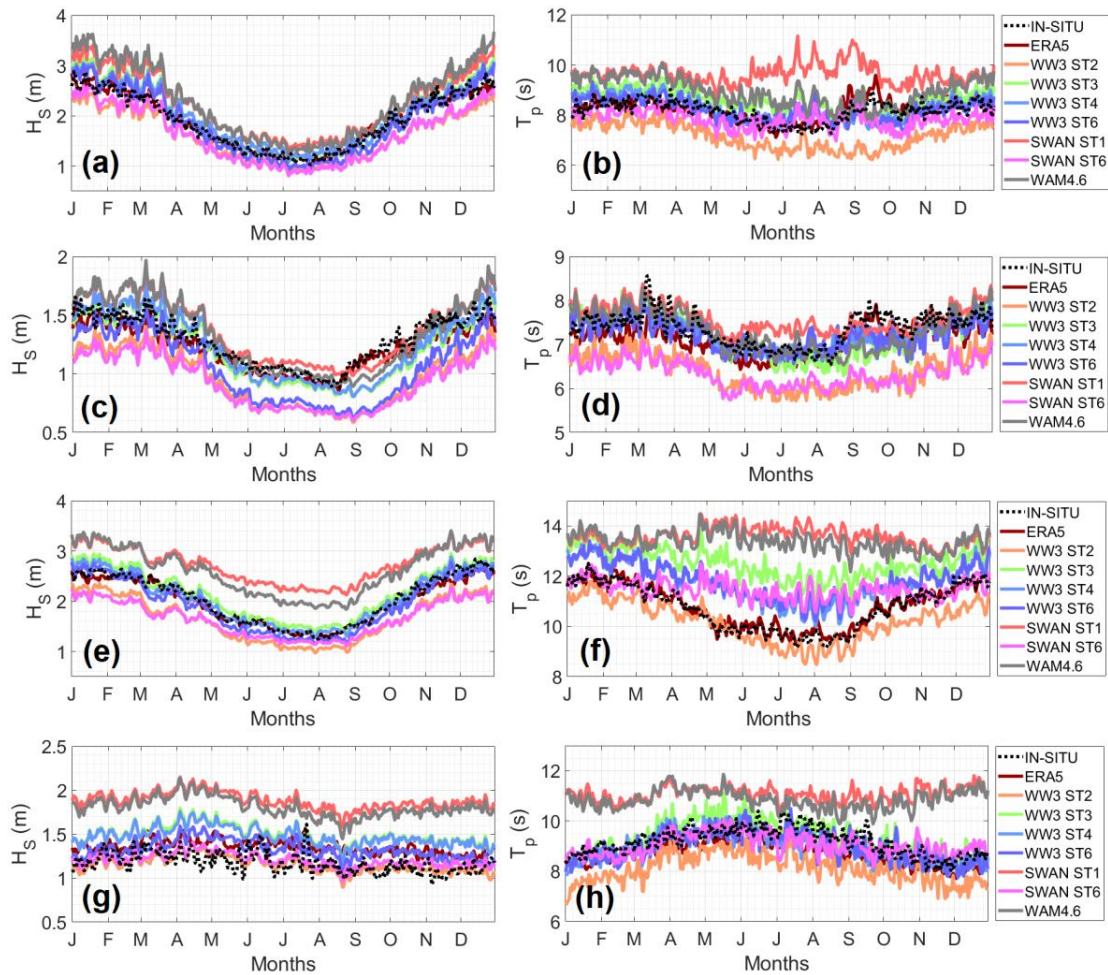
1189
 1190
 1191
 1192
 1193

Figure 5 – Absolute differences (in $^{\circ}$) between the (a) PC20-1 (WW3-ST2) to (g) -7 (WAM4.6) ensemble members' (red arrows) and ERA5 (green arrows) annual mean *MWD* (1995-2014).



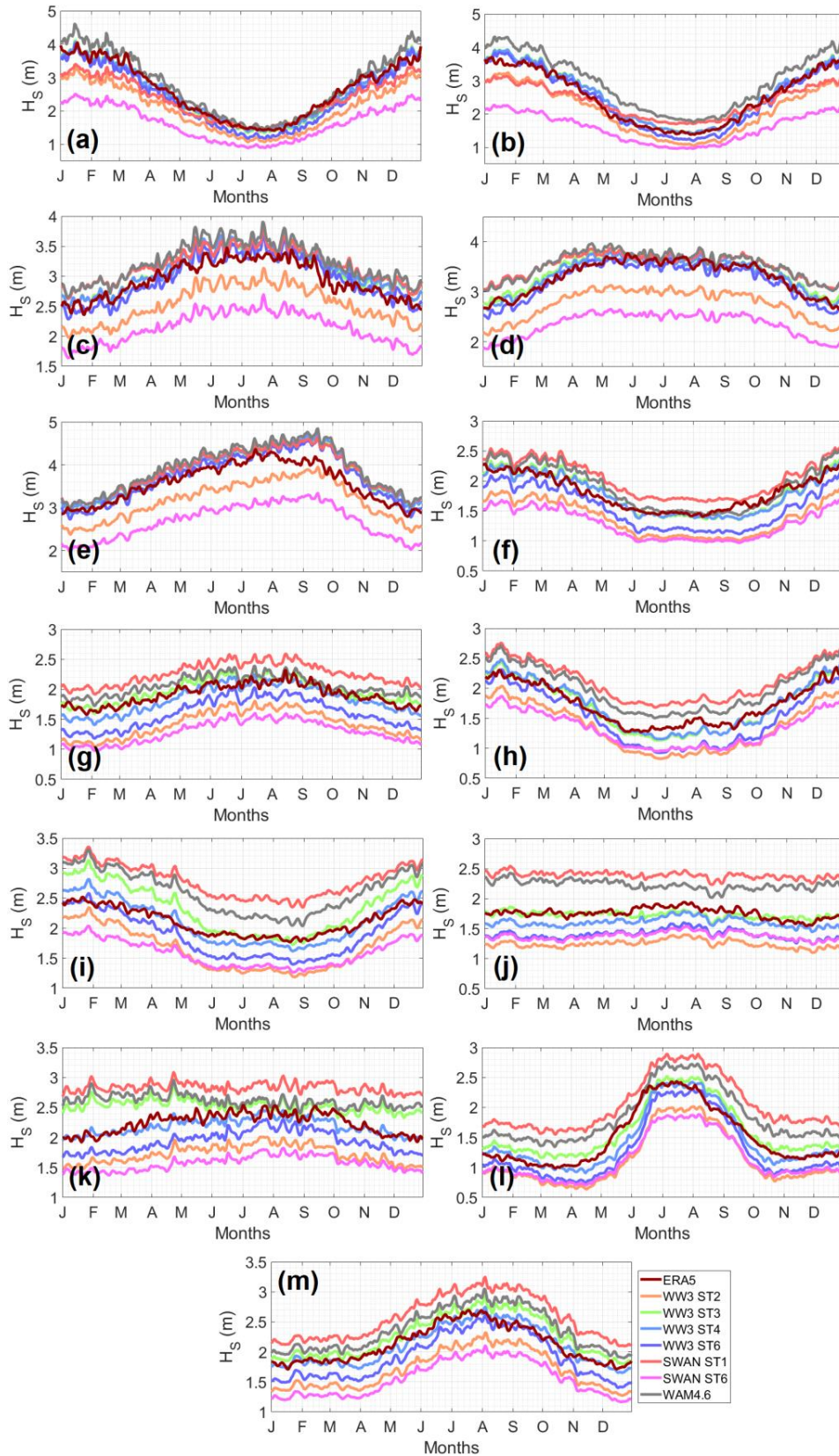
1194
1195
1196
1197
1198
1199
1200

Figure 6 – Merged scatter-QQ-plots from the comparison between *in-situ* multi-year (1995-2014) daily (left) H_s and (right) T_p means, ERA5 and PC20-1 (WW3-ST2) to -7 (WAM4.6) ensemble members at the available *in-situ* locations across (a,b) ETNA, (c,d) TNAO, (e,f) ETNP and (g,h) TWSP/ETSP regional areas. Highlighted percentiles in the QQ-plots refer to the 1%, 10%, 20%, 30%, 40%, 50%, 60%, 70%, 80%, 90%, 95% and 99% ones.



1201
 1202
 1203
 1204
 1205
 1206

Figure 7 – Mean intra-annual (left) H_s and (right) T_p cycles (1995-2014) considering the *in-situ* observations, ERA5 and PC20-1 (WW3-ST2) to -7 (WAM4.6) ensemble members at the available *in-situ* locations across (a,b) ETNA, (c,d) TNAO, (e,f) ETNP and (g,h) TWSP/ETSP regional areas.



1207
 1208
 1209
 1210
 1211

Figure 8 – Mean intra-annual H_s cycles (1995-2014) considering the ERA5 and PC20-1 (WW3-ST2) to -7 (WAM4.6) ensemble members across (a) ETNA, (b) ETNP, (c) ETSA, (d) ETSP, (e) ETSI, (f) TNAO, (g) TSAO, (h) TWNP, (i) TENP, (j) TWSP, (k) TESP, (l) TNIO and (m) TSIO regional areas.

1212

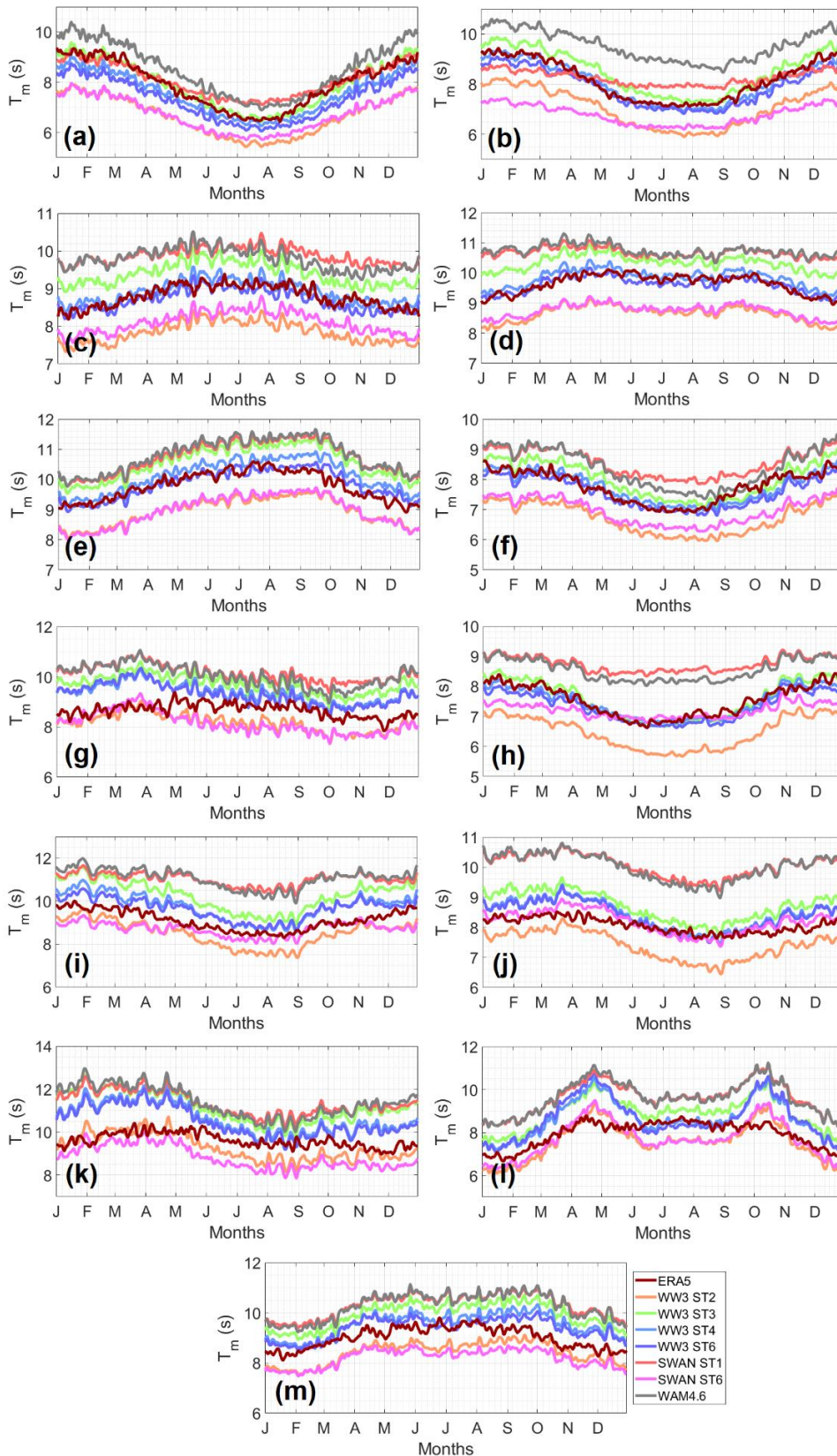
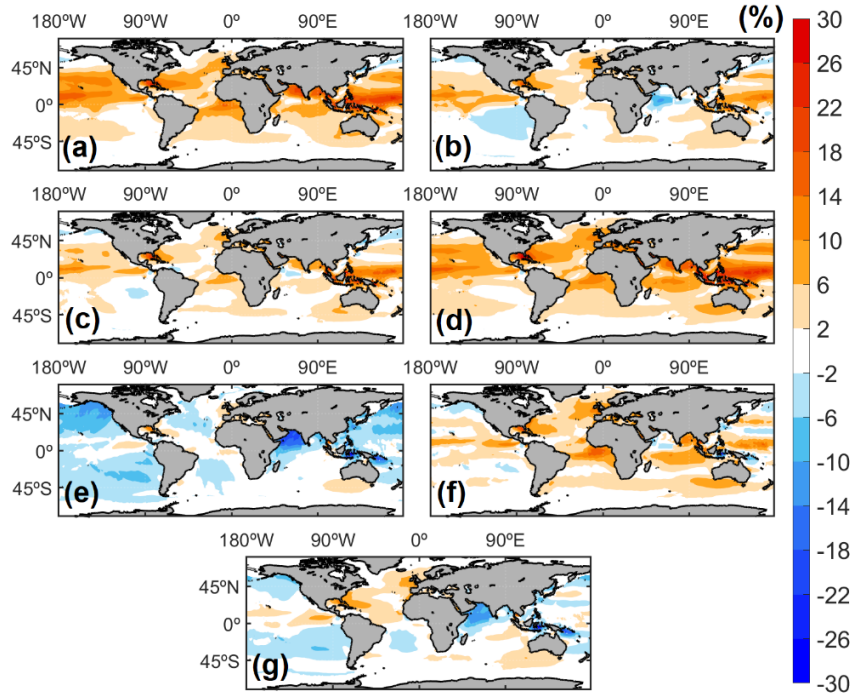


Figure 9 – Same as in Figure 8, but for T_m (s).

1213

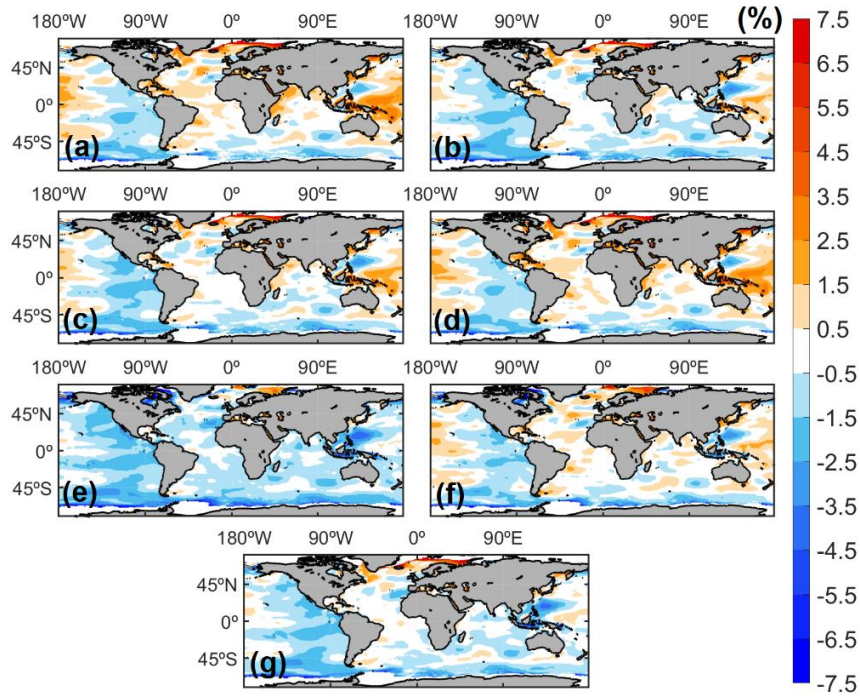
1214

1215



1216
 1217
 1218
 1219

Figure 10 – Normalized differences (in %) between the (a) PC20-1 (WW3-ST2) to (g) - 7 (WAM4.6) H_5 MAVs and ERA5 ones (1995-2014).



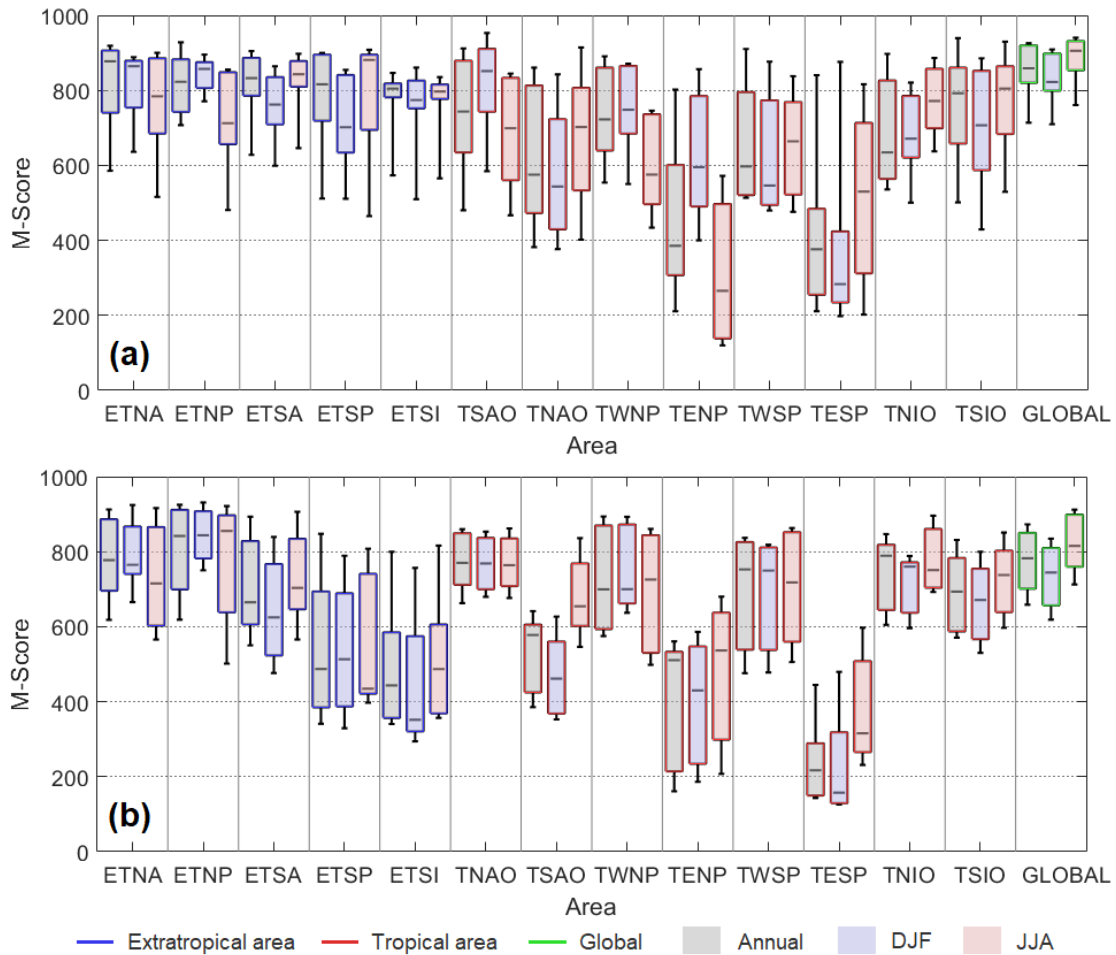
1220

1221

1222

1223

Figure 11 – Normalized differences (in %) between the (a) PC20-1 (WW3-ST2) to (g) - 7 (WAM4.6) H_s IAVs and ERA5 ones (1995-2014).



1224

1225

1226

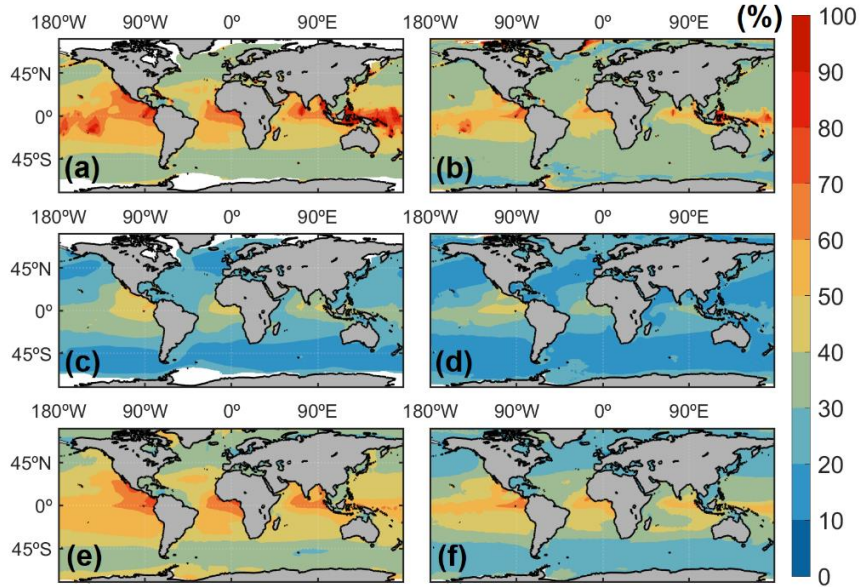
1227

1228

1229

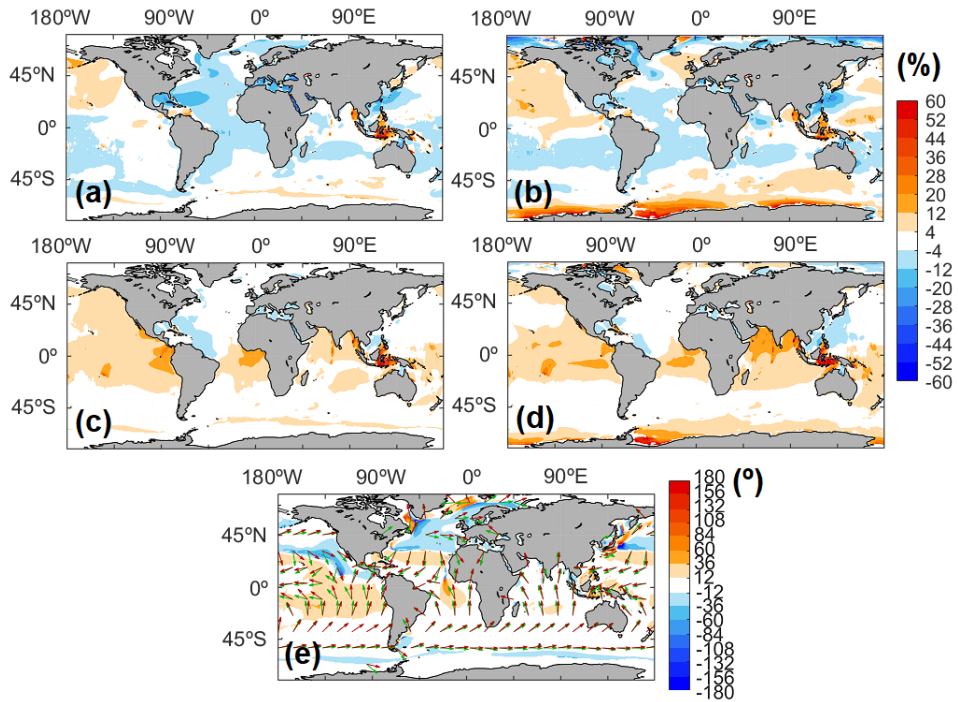
1230

Figure 12 – Boxplots representing the range of (a) H_5 and (b) T_m M-scores within the PC20 ensemble (1995-2014), from the comparison with ERA5, globally and across each of the regional areas. Extratropical areas are outlined in blue, tropical areas in red and the global in green. Grey shading represents the annual boxplots, while blue and red shadings represent DJF and JJA, respectively.



1231
 1232 Figure 13 – Normalized uncertainty range (NUR; in %) for (a,b) the PC20 ensemble, (c,d)
 1233 the WW3 subset of PC20 (*i.e.*, only PC20-1 to -4; ST2 to ST6) and (e,f) the SWAN subset
 1234 of PC20 (*i.e.*, only PC20-5 and -6; ST1 and ST6), considering the annual (left) H_S means
 1235 and (right) 95% percentiles (1995-2014).

1236



1237

1238

Figure 14 – 7-member PC20 full ensemble mean (a-d) normalized (in %) and (e) absolute (in $^{\circ}$) differences in comparison with ERA5, considering the annual mean (a) H_S , (c) T_m and (e) MWD , as well as the annual 95% percentile (b) H_S and (d) T_m (1995-2014).

1240

1241

1242 Table 1 – Statistic metrics representing the PC20-i (1 to 7) performance in representing
 1243 the H_S climate at the selected *in-situ* locations across each area (89 at ETNA, 42 at TNAO,
 1244 84 at ETNP and 22 at TWSP/ETSP).

	ETNA (89)				
	Bias (m)	RMSE (m)	R	SI	Slope
WW3-ST2	-0.29	0.56	0.87	0.30	0.85
WW3-ST3	0.13	0.46	0.87	0.24	1.07
WW3-ST4	0.12	0.46	0.87	0.24	1.06
WW3-ST6	-0.02	0.46	0.87	0.24	0.99
SWAN-ST1	0.37	0.54	0.88	0.29	1.20
SWAN-ST6	-0.27	0.55	0.87	0.29	0.86
WAM4.6	0.41	0.60	0.88	0.32	1.22
	TNAO (42)				
	Bias (m)	RMSE (m)	R	SI	Slope
WW3-ST2	-0.32	0.46	0.83	0.36	0.75
WW3-ST3	-0.07	0.35	0.82	0.27	0.95
WW3-ST4	-0.04	0.34	0.83	0.27	0.97
WW3-ST6	-0.23	0.43	0.82	0.33	0.82
SWAN-ST1	0.09	0.40	0.78	0.31	1.08
SWAN-ST6	-0.36	0.50	0.79	0.39	0.72
WAM4.6	0.06	0.38	0.79	0.29	1.05
	ETNP (84)				
	Bias (m)	RMSE (m)	R	SI	Slope
WW3-ST2	-0.37	0.59	0.90	0.29	0.82
WW3-ST3	0.13	0.38	0.91	0.19	1.06
WW3-ST4	0.04	0.40	0.91	0.20	1.02
WW3-ST6	-0.10	0.44	0.91	0.22	0.95
SWAN-ST1	0.70	0.78	0.84	0.38	1.35
SWAN-ST6	-0.38	0.65	0.87	0.32	0.82
WAM4.6	0.58	0.66	0.88	0.32	1.29
	TWSP / ETSP (22)				
	Bias (m)	RMSE (m)	R	SI	Slope
WW3-ST2	-0.02	0.48	0.79	0.41	0.98
WW3-ST3	0.32	0.43	0.82	0.39	1.27
WW3-ST4	0.30	0.44	0.80	0.38	1.25
WW3-ST6	0.15	0.42	0.81	0.35	1.13
SWAN-ST1	0.70	0.67	0.80	0.57	1.60
SWAN-ST6	0.29	0.50	0.76	0.42	1.02
WAM4.6	0.63	0.62	0.80	0.52	1.54

1245

1246

1247 Table 2 – Summary of PC20-i (1 to 7) H_5 biases (in m) in comparison with *in-situ*
 1248 observations at ETNA, TNAO, ETNP and TWSP/ETSP, at specific percentiles (10%,
 1249 50%, 90%, 95% and 99%).

	ETNA (89)				
	Bias P10%	Bias P50%	Bias P90%	Bias P95%	Bias P99%
WW3-ST2	-0.11	-0.27	-0.52	-0.63	-0.74
WW3-ST3	0.13	0.10	0.14	0.09	0.06
WW3-ST4	0.13	0.10	0.08	0.04	0.01
WW3-ST6	-0.03	-0.05	0.01	-0.04	-0.09
SWAN-ST1	0.34	0.33	0.43	0.39	0.29
SWAN-ST6	-0.09	-0.25	-0.47	-0.58	-0.80
WAM4.6	0.28	0.33	0.61	0.61	0.64
	TNAO (42)				
	Bias P10%	Bias P50%	Bias P90%	Bias P95%	Bias P99%
WW3-ST2	-0.36	-0.29	-0.32	-0.33	-0.35
WW3-ST3	-0.23	-0.04	0.08	0.09	0.16
WW3-ST4	-0.26	-0.0004	0.12	0.12	0.16
WW3-ST6	-0.39	-0.21	-0.08	-0.07	0.02
SWAN-ST1	-0.16	0.08	0.31	0.28	0.54
SWAN-ST6	-0.33	-0.36	-0.39	-0.47	-0.46
WAM4.6	-0.12	0.04	0.24	0.22	0.54
	ETNP (84)				
	Bias P10%	Bias P50%	Bias P90%	Bias P95%	Bias P99%
WW3-ST2	-0.29	-0.38	-0.52	-0.59	-0.63
WW3-ST3	0.05	0.13	0.12	0.12	0.14
WW3-ST4	-0.06	0.02	0.08	0.09	0.13
WW3-ST6	-0.19	-0.14	0.01	0.02	0.06
SWAN-ST1	1.04	0.80	0.41	0.33	0.30
SWAN-ST6	0.05	-0.37	-0.74	-0.84	-0.91
WAM4.6	0.80	0.60	0.47	0.47	0.55
	TWSP / ETSP (22)				
	Bias P10%	Bias P50%	Bias P90%	Bias P95%	Bias P99%
WW3-ST2	0.11	0.02	-0.36	0.08	-0.14
WW3-ST3	0.27	0.38	0.19	0.51	0.40
WW3-ST4	0.26	0.36	0.07	0.51	0.42
WW3-ST6	0.10	0.23	-0.12	0.34	0.29
SWAN-ST1	0.59	0.80	0.62	0.70	0.52
SWAN-ST6	0.26	0.10	-0.37	-0.40	-0.70
WAM4.6	0.62	0.68	0.55	0.65	0.54

1250

1251

1252 Table 3 – Similar to Table 1, but for T_p (s).

	ETNA (24)				
	Bias	RMSE	R	SI	Slope
WW3-ST2	-1.01	1.51	0.72	0.19	0.88
WW3-ST3	0.47	1.17	0.71	0.14	1.06
WW3-ST4	0.11	0.95	0.73	0.12	1.01
WW3-ST6	0.06	1.02	0.69	0.13	1.01
SWAN-ST1	1.49	1.83	0.63	0.22	1.18
SWAN-ST6	-0.31	1.09	0.68	0.13	0.96
WAM4.6	0.77	1.31	0.69	0.16	1.09
	TNAO (39)				
	Bias	RMSE	R	SI	Slope
WW3-ST2	-0.97	1.55	0.75	0.21	0.87
WW3-ST3	-0.17	1.15	0.78	0.16	0.98
WW3-ST4	-0.10	1.02	0.78	0.14	0.99
WW3-ST6	-0.16	1.08	0.77	0.15	0.98
SWAN-ST1	0.24	1.25	0.84	0.17	1.03
SWAN-ST6	-1.02	1.30	0.81	0.18	0.86
WAM4.6	-0.05	1.03	0.82	0.14	0.99
	ETNP (79)				
	Bias	RMSE	R	SI	Slope
WW3-ST2	-0.56	1.18	0.85	0.11	0.95
WW3-ST3	1.78	2.12	0.81	0.20	1.17
WW3-ST4	1.00	1.41	0.86	0.13	1.09
WW3-ST6	1.08	1.49	0.82	0.14	1.10
SWAN-ST1	2.85	3.37	0.68	0.31	1.26
SWAN-ST6	0.72	1.58	0.78	0.15	1.07
WAM4.6	2.63	3.10	0.74	0.29	1.25
	TWSP / ETSP (29)				
	Bias	RMSE	R	SI	Slope
WW3-ST2	-1.09	1.84	0.83	0.20	0.88
WW3-ST3	0.10	1.33	0.88	0.14	1.01
WW3-ST4	-0.25	1.26	0.87	0.14	0.97
WW3-ST6	-0.22	1.28	0.86	0.14	0.98
SWAN-ST1	1.90	2.17	0.80	0.24	1.21
SWAN-ST6	-0.12	1.04	0.84	0.11	0.99
WAM4.6	1.67	2.07	0.75	0.23	1.18

1253

1254

1255 Table 4 – Similar to Table 2, but for T_p (s).

	ETNA (24)				
	Bias P10%	Bias P50%	Bias P90%	Bias P95%	Bias P99%
WW3-ST2	-1.07	-1.20	-0.81	-0.19	-0.16
WW3-ST3	0.15	0.35	1.10	1.74	2.04
WW3-ST4	0.08	-0.06	0.33	1.10	1.37
WW3-ST6	-0.04	-0.09	0.34	1.10	1.29
SWAN-ST1	1.29	1.48	1.96	2.18	2.21
SWAN-ST6	-0.45	-0.40	-0.05	0.40	0.58
WAM4.6	0.53	0.58	1.29	1.99	2.37
	TNAO (39)				
	Bias P10%	Bias P50%	Bias P90%	Bias P95%	Bias P99%
WW3-ST2	-0.62	-1.05	-1.16	-0.94	-0.23
WW3-ST3	-0.56	-0.20	0.20	0.88	1.74
WW3-ST4	-0.30	0.03	-0.14	0.20	1.10
WW3-ST6	-0.42	-0.09	-0.12	0.14	1.11
SWAN-ST1	-0.85	0.68	0.56	1.33	2.28
SWAN-ST6	-1.31	-0.89	-1.07	-0.71	0.44
WAM4.6	-0.52	0.04	0.15	0.84	1.94
	ETNP (79)				
	Bias P10%	Bias P50%	Bias P90%	Bias P95%	Bias P99%
WW3-ST2	-0.27	-0.60	-0.89	-1.01	-1.23
WW3-ST3	1.80	2.00	1.53	1.38	1.11
WW3-ST4	1.05	1.05	0.95	0.86	0.61
WW3-ST6	1.14	1.08	1.02	1.04	0.87
SWAN-ST1	3.33	3.38	1.91	1.60	1.09
SWAN-ST6	1.08	0.89	0.37	0.30	0.18
WAM4.6	2.80	3.11	1.96	1.71	1.30
	TWSP / ETSP (29)				
	Bias P10%	Bias P50%	Bias P90%	Bias P95%	Bias P99%
WW3-ST2	-0.09	-1.66	0.02	-0.15	-0.38
WW3-ST3	-0.84	-0.22	2.03	2.02	1.95
WW3-ST4	-0.40	-0.69	1.45	1.52	1.45
WW3-ST6	-0.25	-0.70	1.42	1.47	1.33
SWAN-ST1	2.82	1.61	2.21	1.99	1.83
SWAN-ST6	0.49	-0.47	0.40	0.33	0.09
WAM4.6	2.68	1.21	2.42	2.20	2.00

1256

Performance Evaluation of a Global CMIP6 Single Forcing, Multi Wave Model Ensemble of Wave Climate Simulations – Highlights

- A performance evaluation of a new CMIP6 ensemble of wave climate simulations
- Ensemble architecture focused on model-parameterization-induced uncertainties
- Evaluation through comparison with ERA5 and an extensive *in-situ* observational set
- Ensemble spreads found to exceed even high-end projected change rates until 2100

Performance Evaluation of a CMIP6 Single Forcing, Multi Wave Model Ensemble of Wave Climate Simulations

AUTHOR STATEMENT

Gil Lemos: Conceptualization, Methodology, Software, Formal Analysis, Writing – Original Draft

Alvaro Semedo: Conceptualization, Methodology, Validation, Investigation, Supervision

Rajesh Kumar: Conceptualization, Software, Validation, Investigation, Resources,

Mikhail Dobrynin: Software, Investigation, Resources

Adem Akpinar: Software, Investigation, Resources, Writing – Review & Editing

Bahareh Kamranzad: Software, Investigation, Resources

Jean Bidlot: Resources, Data Curation

Hector Lobeto: Validation, Data Curation, Writing – Review & Editing

Declaration of interests

The authors declare that they have no known competing financial interests or personal relationships that could have appeared to influence the work reported in this paper.

The authors declare the following financial interests/personal relationships which may be considered as potential competing interests:

Journal Pre-proof